UNIVERSITY OF CALGARY

Observation and characterization of electromagnetically induced transparency using evanescent fields

by

Ryan James Thomas

A THESIS
SUBMITTED TO THE FACULTY OF GRADUATE STUDIES
IN PARTIAL FULFILLMENT OF THE REQUIREMENTS FOR THE
DEGREE OF MASTER OF SCIENCE

DEPARTMENT OF PHYSICS AND ASTRONOMY

INSTITUTE FOR QUANTUM INFORMATION SCIENCE

CALGARY, ALBERTA

September, 2012

UNIVERSITY OF CALGARY

FACULTY OF GRADUATE STUDIES

The undersigned certify that they have read, and recommend to the Faculty of Graduate Studies for acceptance, a thesis entitled "Observation and characterization of electromagnetically induced transparency using evanescent fields" submitted by Ryan James Thomas in partial fulfillment of the requirements for the degree of MASTER OF SCIENCE.

Supervisor, Dr. Alexander Lvovsky
Department of Physics and Astronomy

Dr. Christoph Simon
Department of Physics and Astronomy

Dr. Wolfgang Tittel
Department of Physics and Astronomy

Dr. Belinda Heyne
Department of Chemistry

Date

Abstract

We investigate Electromagnetically Induced Transparency (EIT) induced by evanescent fields generated through selective reflection at an interface of glass and hot rubidium vapor. We observe a distinct transmission window corresponding to EIT for incident angles above the critical angle for total internal reflection (TIR). This is a surprising result, as the size of the interaction region is on the order of microns, and one would expect the motion of atoms to destroy the EIT phenomenon. The transmission window exhibits a sharp cusp whose width is limited to about 1 MHz – less than the natural width of the atomic transition and thus strong evidence for EIT. We develop an analytical model to describe our observations where the cusp is due to a depth-dependent atomic susceptibility, and we show that our model provides reasonable agreement with the observed spectra. Deviations of the theory from the data are discussed. We show that the width of the transmission window is independent of the size of the interaction region, which indicates that the main source of decoherence is likely due to collisions with the interface rather than diffusion of atoms or Rb-Rb spin-exchanging collisions. Applications of this system to compact optical frequency standards and comparisons with current EIT based optical clocks are discussed. A theoretical discussion of the Goos-Hänchen effect in the presence of EIT is presented and compared with measured data.

Acknowledgements

Following the suggestion of a colleague, I will keep the acknowledgements simple: I don't owe nobody nothing.

Before the reader attempts to parse the loopholes of logic posed by that seemingly innocuous statement, I should say that the simplest interpretation of that statement – that there is no one to whom I owe thanks – is completely false. In the past two years I have learned a great deal of physics, both experimental and theoretical, and I would have only learned a small of fraction of it without the assistance of others. And while at many points during my degree I have been incredibly frustrated and unhappy with my work, it has been for the most part a very enjoyable experience. In this section I would like to thank – in no particular order – the people who made this thesis possible and contributed to my enjoyment of of my degree.

I suppose the first person I should thank is my supervisor, Alex Lvovsky. Certainly we have butted heads over the past two years, and as a result we consider the other to be arrogant, but I must admit that I have learned a great deal of physics from him. If there is anything I hope that I have picked up from Alex, it is his occasional ability to come up with brilliantly simple solutions to technical problems. I must also thank Alex for the supportive, if unrealistic, reference letters he has written for me for scholarships and industry positions.

Most of the assistance on the experiment came from Connor Kupchak. I worked with him on his project (at that point it was a joint project) for a year and a half, and I picked up a lot of practical aspects of experimental physics from him. When I started on the project in this thesis, Connor diverted nearly two months of his time to helping me with the initial stages at the cost of not working on his own thesis. Well, it is not like he had a choice with a broken laser! Without his help, I would have taken much longer to finish the project.

I may have finished my thesis a couple of months earlier if it had not been for the presence and distractions of (now Dr.) Andrew Macrae. However, if Andrew had not been around it is safe to say that this thesis would have never been written, I would have never stayed in graduate school, and I would know far less than I do now. A good three-quarters of the knowledge that I obtained from other people during my degree came from Andrew. He was able to help me out with innumerable problems, and I particularly enjoyed our informal discussion of physics related and unrelated to our current experiments. I think I probably delayed *his* thesis defence by a couple of months with my constant pestering! All his considerable professional contributions aside, I am also grateful for his friendship, and my life has been much richer having known him.

I am equally grateful to Pantita Palittapongarnpim, whose dedication and passion for her work has been a source of inspiration for me. I thank her for her help, whether just to act as a sounding board for problems, to provide suggestions, or even as an occasional extra pair of hands. I thank her for her patience with me, and for her sincerity when telling me exactly what she thinks. I thank her for all the long and very interesting conversations about incredibly random subjects. But most of all, I thank her for her friendship; a friendship that means more to me than I can possibly convey.

There are others I should thank, but I am running out of room here and becoming overly sentimental. So let it be said that I thank, to an equal or lesser extent, the following people for their suggestions, help, and distractions: Andal Narayanan, Ranjeet Kumar, Travis Brannan, and Aimee Heinrichs. Every one of you made the time I spent on my degree more enjoyable, and for that I am most grateful.

For all the discussions, the distractions, the time lost to vortices of procrastination; for all the successes, the frustations, and the laughter; for the sense of belonging, the sense of community, the camaraderie. For all this and more, I dedicate this thesis, such as it is, to my friends.

Table of Contents

List of Figures and Illustrations

Chapter 1

Introduction

In this thesis, I shall describe an experiment which investigates electromagnetically induced transparency (EIT) induced by evanescent optical fields in a hot atomic vapour. Before I explain why this is interesting, I shall describe why EIT itself is interesting and useful.

The phenomenon of EIT is a well-known non-linear optical effect whereby the interaction of two optical fields with an appropriately chosen atomic system results in a narrow transparency window for one of the optical fields. The effect was first observed by Boller *et al.* [2] in 1991 using a hot gas of neutral strontium atoms. Since then, the number of systems where EIT and analagous coherent effects have been observed has increased drastically. In addition to warm atomic vapours, EIT has been observed in solid-state systems [3], superconducting qubits [4, 5], and optomechanical architectures [6, 7, 8]. Broadly speaking, EIT has attracted a great deal of interest for two related applications: quantum memories and photon-photon gates. Light pulses can be trapped inside an EIT medium as an atomic excitation and then reversible mapped back into a propagating optical excitation some time later [9, 10]. The non-linearity associated with EIT can also be used for photon-photon gates; in particular, it can be used as a controlled phase gate (eg. Schmidt and Imamoğlu [11]) which is a universal quantum gate [12]. EIT can also be achieved with guided, rather than free space, fields, and this has both practical advantages for long-distance quantum communication and theoretical advantages for increasing gate fidelity [13]. In particular, nano-fibers [14] offer a convenient method for interacting bulk EIT media with guided modes via evanescent fields [15]. Nano-fibers also have several other interesting features that makes them worthy of study. As the fiber diameter is smaller than the wavelength of light, it is possible to obtain very high light intensities even for very low light levels. The higher intensity of the light, the stronger the light couples to atomic systems; this effect is what makes nano-fibers particularly attractive for quantum gates. Non-linear optical effects have already been observed with nano-fibers embedded in hot atomic vapour at the 10 nW level [16]. An additional advantage of the evanescent fields from nano-fibers is that they can be used to trap atoms in a two-color dipole trap [14].

EIT has also garnered interest as an optical frequency reference [17]. The EIT transmission window is created only at the two-photon resonance, and in typical experiments with akali metal atoms this means that the frequency difference between the two optical fields is on the order of a few gigahertz. In comparison, the EIT linewidth can be extremely narrow: tens of kilohertz are easily obtained in typical EIT experiments using buffer gas and moderate control field intensities, while in paraffin coated vapour cells the EIT linewidth can reach the level of about 100 Hz [18]. While the frequency stability of such clocks is far worse than that of hydrogen masers and cesium fountains, clocks based on EIT can be used as compact and transportable references [17, 19, 20].

Our method of observing EIT in evanescent fields is to create the fields using total internal reflection from an interface of glass and hot atomic vapour. This particular spectroscopic technique is known as selective reflection [21, 22, 23]. Selective reflection is interesting in its own right, as it allows one to probe the transient response of atoms when they collide with the interface [24]. It is also a useful technique for probing the spectral properties of dense atomic vapours [25]. Total internal reflection from two dielectrics also gives rise to the Goos-Hänchen shift, where the lateral and angular position of a totally reflected light beam of finite size is shifted relative to the expectation from geometrical optics [26, 27]. When there is a dense atomic vapour as one of the dielectrics a frequency-dependent modification of the beam shift appears [28].

So why is EIT in evanescent fields interesting? I shall give three reasons, in order of importance. First, our method of investigating EIT in evanescent fields using selective reflection is much simpler than implementing a nano-fiber system in either warm or cold atomic vapour.

While we cannot study the propagation characteristics of nano-fibers nor can we trap atoms with our system[1], it still allows us to study many of the same spectroscopic phenomenon with greater ease. Second, the system has potential as a compact optical clock. The length scale of the evanescent fields is on the order of an optical wavelength, so in principle one could build an optical clock at the micro-metric scale. Of course, current laser and electronics technology would ultimately limit the size to be above the micro-metric scale. Such a clock would be both transportable and extremely compact, and it could potentially be used as a magnetometer with micrometric resolution. Third, and most importantly, achieving EIT in such a small interaction region is a very surprising result. One would expect the motion of the atoms and collisions with the interface to completely wash out the EIT phenomenon, and yet this is not observed. This is similar to work that has been done with EIT in micro-metric and nano-metric thin cells, where a warm atomic vapour is confined in one direction to lengths on the order of a micron [31, 32, 33, 34]. One would expect collisions with the walls in the short dimension to wash out the EIT transmission peak, but only atoms that fly parallel to the walls contribute to EIT formation. Thus, when we restrict our interaction regions to microscopic sizes new and interesting physics appears. One theoretical example of this is the potential for enhanced Goos-Hänchen shifts in Doppler broadened vapours under EIT conditions due to the necessity of phase-matching between the probe and control fields. To investigate new and interesting physics is itself a sufficient reason alone to study EIT in evanescent fields.

This thesis is organized as follows. Chapter 2 discusses the basic theory behind the experiment. A significant amount of the work in this thesis was in developing a theory that accounts for the observed EIT spectra. Both EIT and Maxwell's equations are briefly reviewed, and then a discussion of the problem of selective reflection is presented. Some limitations of the basic model are explained, and extensions are proposed. A discussion of the classic Goos-Hänchen shift is presented along with an analysis of the effect under EIT conditions with a Doppler

---

[1] It is, however, possible to trap *cold* atoms with evanescent fields near a surface [29, 30]

broadened gas and the potential increase in the shift.

Chapter 3 outlines the experimental apparatus. The choice and properties of the atomic system, as well as the system used to generate evanescent fields, are discussed. Our methods for measuring the phase profile and beam shift are also presented.

Chapter 4 details the measurements of the interface reflectivity and comparisons with the theoretical model developed in Chapter 2, and deviations from the basic theory are discussed. Further characteristics of the EIT spectra are presented, and those results are used to show that diffusion of atoms does not play an important role in the decoherence mechanisms of our system. Finally, a measurement of the Goos-Hänchen shift is presented in the presence of EIT.

Finally, Chapter. 5 summarizes the work that has been presented and discusses improvements to and applications of the experimental system.

Chapter 2

Theory

About half of the work in this thesis was developing a theory that would describe the effect of EIT in evanescent fields. That theory is described in this chapter. The following two sections will outline the physics of EIT and the behaviour of electromagnetic waves at dielectric interfaces. I realize that to some this is basic physics, but it will help to establish nomenclature and conventions. The subsequent sections will derive the theory that will be used for the remainder of the thesis.

2.1 Electromagnetically induced transparency (EIT)

In this thesis, the quantum system of interest is an ensemble of three-level atoms in a Λ-configuration as shown in Fig. 2.1. We have two ground-state levels with no dipole allowed transition between them, labelled $|b\rangle$ and $|c\rangle$, and a single excited state which has a dipole allowed transition with each ground state, labelled $|a\rangle$. We have two optical fields, a probe and a control field, which couple transitions $|b\rangle - |a\rangle$ and $|c\rangle - |a\rangle$, respectively. The control field is

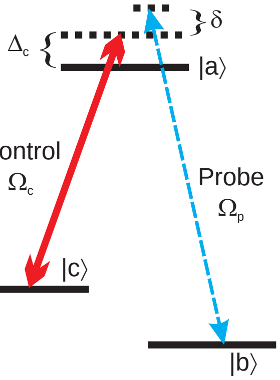

Figure 2.1: Level scheme for EIT with a Λ-type three level system.

detuned from resonance by an amount Δ_c, and the probe field is detuned from the control field by an amount δ. The Hamiltonian that describes this system is, in the interaction picture and rotating wave approximation,

$$H = -\hbar \begin{pmatrix} \Delta_c + \delta & \Omega_p & \Omega_c \\ \Omega_p^* & 0 & 0 \\ \Omega_c^* & 0 & \delta \end{pmatrix} \tag{2.1}$$

where the coupling of the probe and control fields are described by their respective Rabi frequencies, defined as $\Omega = \vec{E} \cdot \vec{d}/\hbar$ [35]. Here, $\vec{d}$ is the dipole matrix element and $\vec{E}$ the electric field vector. Under the condition that $\delta = 0$, this Hamiltonian has as one of its eigenstates the so-called dark state [36]

$$|\psi\rangle = \frac{\Omega_c|b\rangle - \Omega_p|c\rangle}{\sqrt{\Omega_c^2 + \Omega_p^2}} \tag{2.2}$$

which has no component of the excited state and therefore does not couple to the optical fields. This means that a collection of atoms that have this Hamiltonian will quickly be pumped into a state that is transparent to both optical fields. In the absence of ground state relaxation mechanisms, the atoms will remain there indefinitely. This effect is called coherent population trapping (CPT). EIT is a special case of CPT, where we require that Ω_p be much less than all other Rabi frequencies and dephasing rates, so the dark state is simply the state $|b\rangle$.

In any real atomic system, spontaneous emission and other dephasing processes destroy pure states such as Eq. (2.2). In order to have a full description of EIT, I must include those effects too. I use the density matrix formalism and the master equation

$$\partial_t \rho = \frac{i}{\hbar}[\rho, H] + (\partial_t \rho)_{decay} \tag{2.3}$$

to determine the state of the system, where $(\partial_t \rho)_{decay}$ describes the rate of change of the density matrix elements due to spontaneous decay and ground state dephasing. A common method for determining the effect of damping is the Lindblad formalism [36] which includes damping using a superoperator of the form

$$(\partial_t \rho)_{\text{decay from } j\to i} = \frac{\Gamma}{2}(2\sigma_{ij}\rho\sigma_{ji} - \sigma_{ji}\sigma_{ij} - \rho\sigma_{ji}\sigma_{ij}) \tag{2.4}$$

where $\sigma_{ij} = |i\rangle\langle j|$ and Γ is a decoherence rate. The master equation can be used to determine the temporal dynamics of the system, and has been used succesfully in describing stopped light experiments in EIT [35]. My task is simplified because in this thesis only the steady-state response of the system to the optical fields is relevant. Once the steady-state density matrix is known, I calculate the polarization of the atoms as $P = Nd\rho_{ab}$ where N is the number density of atoms. The susceptibility for plane wave fields, defined through $P = \epsilon_0\chi E$, is [36]

$$\chi = \frac{Nd^2}{\hbar\epsilon_0}\frac{\delta + i\gamma}{|\Omega_c|^2 - (\delta + i\gamma)(\Delta_c + \delta + i\Gamma/2)} \tag{2.5}$$

where γ is the relaxation rate of the ground state coherence (no population exchange) and Γ is the relaxation rate of the ground-excited state coherence. In this thesis, Γ is the sum of both the natural linewidth and the collisional broadening. The susceptibility is plotted in Fig. 2.2. Note that the narrow transmission window is accompanied by steep normal dispersion as required by the Kramers-Kronig relations. The steep dispersion gives rise to a very slow group velocity,

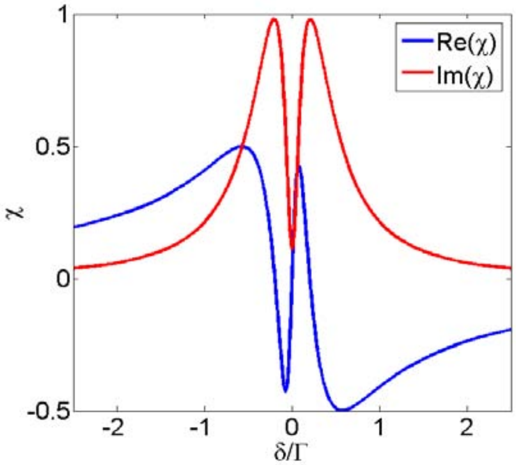

Figure 2.2: Real and imaginary parts of the susceptibility as given in Eq. (2.5) in the presence of the control field.

the magnitude of which can be varied with the control field. If the control field is turned off as a pulse propagates through an EIT medium then it is possible to stop the optical pulse inside the EIT medium. If the control field is turned back on again the pulse will re-accelerate and leave the medium. What makes this possible is that when the optical field is in the atomic vapour the optical and atomic state combine to form a *dark state polariton* [9], where the contribution of each part to the polariton is determined by the control field strength. For $\Omega_c = 0$ the polariton is purely atomic, and when $\Omega_c \neq 0$ the polariton is a combination of optical and atomic parts. Thus, when there is no control field present the atom-light state becomes purely atomic and is therefore stationary. This is what allows reversible mapping of optical states into and out of EIT media.

The above theory for EIT neglects an important effect that is present in warm atomic vapours: the motion of the atoms. From the perspective of a single atom, its velocity with respect to the direction of propagation of the probe and control fields will cause the apparent frequencies of the light fields to shift due to the Doppler effect. These frequency shifts differ between each atom and lead to inhomogeneous broadening of the natural line. Contrast this to collisional broadening which is homogeneous as it affects all atoms the same way. The standard way to account for this effect is to replace Δ_c with $\Delta_c - \vec{k}_c \cdot \vec{v}$, where $\vec{k}_c$ is the wavevector of the control field and $\vec{v}$ is the velocity of the atom, and δ with $\delta - (\vec{k}_p - \vec{k}_c) \cdot \vec{v} = \delta - \Delta\vec{k} \cdot \vec{v}$ ($\vec{k}_p$ being the wavevector of the probe field). One then integrates Eq. (2.5) over a Maxwellian distribution of velocities (here I restrict this discussion to one dimension)

$$P(v_z)dv_z = \left(\frac{m}{2\pi k_B T}\right)^{1/2} \exp(-\frac{m v_z^2}{2k_B T})dv_z = \frac{1}{\sqrt{2\pi v_T^2}} \exp(-\frac{v_z^2}{2v_T^2})dv_z \tag{2.6}$$

which gives the probability of an atom having a velocity v_z. Generally, such integrals cannot be expressed in terms of elementary functions[1], so I instead follow Javan *et al.* [37] and Figueroa *et al.* [38] and approximate the Gaussian in Eq. (2.6) by a Lorentzian with the same height and

---

[1] Technically, this integral can be expressed in terms of the Faddeeva function, but this adds little to the discussion.

width

$$P(v_z)dv_z \approx \frac{1}{\sqrt{2\pi}v_T}\frac{1}{1+\frac{v_z^2}{2v_T^2}}dv_z. \tag{2.7}$$

This is technically not a probability distribution, as it is no longer normalized, but given that the Doppler width $k_p v_T$ is typically $180 - 200$ MHz compared to natural linewidths on the order of 10 MHz it is a suitable approximation near resonance. Besides, one can actually calculate the convolution of Eqs. (2.5) and (2.7) without resorting to special functions: the result is

$$\chi = \frac{Nd^2\sqrt{\pi}}{\hbar\epsilon_0}\frac{\delta + i\gamma'}{|\Omega_c|^2 - (\delta + i\gamma')(\Delta_c + \delta + i\Gamma'/2)} \tag{2.8}$$

where $\Gamma' = \Gamma + 2\sqrt{2}k_p v_T$ and $\gamma' = \gamma + \Delta k v_T$. It is a convenient twist of fate that the form of the EIT lineshape is invariant under the convolution. Note that most studies do not consider the effect of the wavevector mismatch on the EIT lineshape for Λ-level schemes. There are two reasons for this. The first is that the wavevector mismatch is generally very small for co-propagating beams and small hyperfine splittings, and the residual Doppler broadening of the two-photon resonance is on the order of kilohertz. The second reason is that EIT experiments are often performed with buffer gas in addition to the active atoms. Buffer gas acts to reduce the effect of wavevector mismatch by the process of Dicke-narrowing [39], so I shall set $\gamma' = \gamma$.

Counterintuitively, Doppler broadening actually leads to a reduction in the EIT width. Since the form of the susceptibility is unchanged for stationary atoms as opposed to Doppler broadened atoms, the expression for the EIT width [38]

$$\text{FWHM} = 2\gamma + 4\frac{\Omega_c^2}{\Gamma'} \tag{2.9}$$

is still valid even though I use Γ' instead of Γ. This expression for the EIT width will become important when I discuss evanescent EIT.

2.2 Maxwell's equations, boundary conditions, and Fresnel equations

In the previous section I outlined the effect that light has on three-level atoms in a Λ-configuration. Now I want to do the opposite: elaborate how the atoms affect the optical fields. The effect that the atoms have on the optical fields is determined by Maxwell's equations. In non-magnetic matter and in the absence of free charges and currents, Maxwell's equations can be written as [40]

$$\nabla \cdot \vec{D} = 0 \tag{2.10a}$$

$$\nabla \cdot \vec{B} = 0 \tag{2.10b}$$

$$\nabla \times \vec{E} = -\dot{\vec{B}} \tag{2.10c}$$

$$\nabla \times \vec{B} = \mu_0 \dot{D} \tag{2.10d}$$

where $\vec{B}$ is the magnetic field, μ_0 is the permeability of free space, and the upper dot indicates a time derivative. The electric displacement $\vec{D}$ is

$$\vec{D} = \epsilon_0 \vec{E} + \vec{P} \tag{2.11}$$

where ϵ_0 is the permittivity of free space and $\vec{P}$ is the polarization. In general, $\vec{B}$, $\vec{E}$, and $\vec{P}$ are functions of both position and time. The electromagnetic wave equation can be derived by taking the curl of Eq. (2.10c), the time derivative of Eq. (2.10d) and using Eq. (2.11) to get

$$\nabla^2 \vec{E} - \frac{1}{c^2}\ddot{\vec{E}} = \frac{1}{\epsilon_0 c^2}\ddot{\vec{P}} - \frac{1}{\epsilon_0}\nabla(\nabla \cdot \vec{P}) \tag{2.12}$$

where, as usual, $c = (\epsilon_0 \mu_0)^{-1/2}$ is the speed of light in a vacuum. In this thesis, I am only concerned about the case where the electric fields are harmonic with angular frequency ω and have a harmonic time-dependence $e^{-i\omega t}$, so I can immediately eliminate time derivatives and obtain

$$(\nabla^2 + \frac{\omega^2}{c^2})\vec{E} = -\frac{\omega^2}{\epsilon_0 c^2}\vec{P} - \frac{1}{\epsilon_0}\nabla(\nabla \cdot \vec{P}). \tag{2.13}$$

In the special case that we have a homogenous, isotropic, linear medium where $\vec{P} = \epsilon_0 \chi \vec{E}$ (χ is thus a constant scalar) Eq. (2.13) can be simplified to

$$(\nabla^2 + \frac{\omega^2}{c^2}(1+\chi))\vec{E} = 0 \tag{2.14}$$

and the index of refraction n can be immediately be identified as $n = \sqrt{1+\chi}$.

From Maxwell's equations, one can derive a set of boundary conditions that the electric and magnetic fields must obey at an interface of two non-magnetic media. The derivation of the boundary conditions can be found in [40], and they are

$$n_1^2 E_1^{\perp} = n_2^2 E_2^{\perp} \tag{2.15a}$$

$$\vec{E}_1^{||} = \vec{E}_2^{||} \tag{2.15b}$$

$$\vec{B}_1 = \vec{B}_2 \tag{2.15c}$$

where $\perp$ denotes the component of the field that is perpendicular to the interface and $||$ denotes the components that are parallel to the interface. The magnetic field is irrelevant here except for how it determines the electric field at the boundary, so by using Eq. (2.10c) and the assumption of harmonic time dependence I can replace the magnetic field with $\vec{B} = \frac{i}{\omega}\nabla \times \vec{E}$.

Now that I have the boundary conditions, I want to determine what happens to an incident plane wave at the interface of two semi-infinite, homogenous, isotropic, linear media. It is worth spelling out the exact problem now, as I will return to it when I discuss the case of selective reflection from an atomic vapour. Consider the situation in Fig. 2.3. Let us assume that we have an incident plane wave given by $\vec{E}_1(\vec{r}) = \vec{E}_1 e^{i\vec{k}_1 \cdot \vec{r}}$ where $\vec{E}_1$ is the complex amplitude of the incident field and $\vec{k}_1$ is the wavevector of the incident field. I similarly define the reflected field $\vec{E}_2(\vec{r})$ and the transmitted field $\vec{E}_3(\vec{r})$ and their respective wavevectors. I assume that my interface is in the $x-y$ plane, and that my incident field propagates in the $x-z$ plane at an angle θ with the z-axis. In that case, the incident wavevector is given by $\vec{k}_1 = n_1 k_0(\sin\theta \hat{x} + \cos\theta \hat{z}) = n_1 k_0(a\hat{x} + b\hat{z})$ where I have defined $k_0 = \omega/c$. By the law of

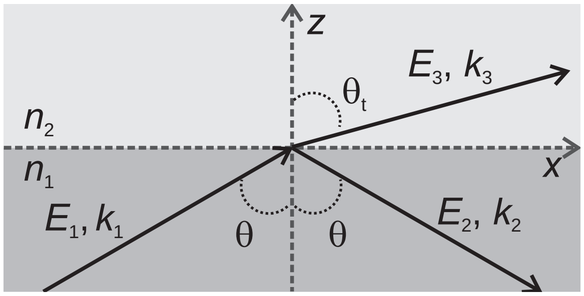

Figure 2.3: Reflection and transmission at a boundary between two different dielectrics.

reflection, the reflected wavevector is given by $\vec{k}_2 = n_1 k_0(a\hat{x} - b\hat{z})$, and by Snell's law

$$n_1 \sin\theta = n_2 \sin\theta_t \tag{2.16}$$

the transmitted field has a wavevector $\vec{k}_3 = n_2 k_0(\sin\theta_t \hat{x} + \cos\theta_t \hat{z})$ where $\cos\theta_t = \sqrt{n_2^2 - n_1^2 \sin^2\theta}$. The relationship between the wavevectors arises due to the fact that the boundary conditions given by Eq. (2.15) have to hold at all points along the boundary. The relationships between the electric fields on either side of the boundary depend on the polarization of the field, as evidenced by the fact that Eqs. (2.15a) and (2.15b) are for polarizations parallel and perpendicular to the interface. In this thesis, I will deal only with the case of polarization perpendicular to the plane of incidence. In that case, the boundary conditions take the form of the Fresnel equations for the reflected and transmitted fields [41]

$$\vec{E}_2 = \frac{n_1\cos\theta - \sqrt{n_2^2 - n_1^2\sin^2\theta}}{n_1\cos\theta + \sqrt{n_2^2 - n_1^2\sin^2\theta}}\vec{E}_1 = r\vec{E}_1 \tag{2.17a}$$

$$\vec{E}_3 = \frac{2n_1\cos\theta}{n_1\cos\theta + \sqrt{n_2^2 - n_1^2\sin^2\theta}}\vec{E}_1 = t\vec{E}_1. \tag{2.17b}$$

If one is interested in energy transport between the media, then one needs to calculate the z-component of the Poynting vector as

$$\vec{S}\cdot\hat{z} = \frac{\epsilon_0 c^2}{2}\Re(\vec{E}\times\vec{B}^*)\cdot\hat{z} = \frac{\epsilon_0 c}{2\omega}|\vec{E}|^2\Re(\vec{k}^*\cdot\hat{z}), \tag{2.18}$$

and then one can define the reflectivity $R = \frac{\vec{S}_2\cdot\hat{z}}{\vec{S}_1\cdot\hat{z}} = |r|^2$ and transmisivity $T = \frac{\vec{S}_3\cdot\hat{z}}{\vec{S}_1\cdot\hat{z}} = |t|^2\Re\left(\frac{\cos\theta_t}{\cos\theta}\right)$. Now there is an interesting bit of physics that comes from this definition of energy transport. In the case that $n_2 < n_1$ it is possible to have the incident field at angles such that $\sin\theta_t > 1$. When this occurs we also have that $\cos\theta_t$ is imaginary, so the transmitted electric field is

$$\vec{E}_3(\vec{r}) = \vec{E}_3 \exp\left(i n_1 k_0 x \sin\theta - n_2 k_0 z \sqrt{\left(\frac{n_1}{n_2}\right)\sin^2\theta - 1} \right). \tag{2.19}$$

Instead of having a travelling wave that penetrates and carries energy into the second medium, we have an *evanescent* wave that travels parallel to the interface and decays exponentially into the second medium. Furthermore, the evanescent wave does not transport energy into the second medium, since the z-component of its wavevector is purely imaginary and Eq. (2.18) requires a real wavevector. Note also that the magnitude of the reflection coefficient in Eq. (2.17a) is now unity. This is the effect of total internal reflection (TIR).

2.3 Selective reflection

In this section, I will attempt to formally state the problem of selective reflection as it applies to this thesis. In the next couple of sections, I will then proceed to solve it using the Green's function method.

The statement of the problem follows Fig. 2.3. I consider two semi-infinite media which have an interface in the $x - z$ plane; the region $z < 0$ has a linear, homogeneous, isotropic dielectric with index of refraction n_1, and the region $z > 0$ contains an atomic vapour of three-level atoms in a Λ-configuration as shown in Fig. 2.1. Two electromagnetic plane waves are incident on the surface with wavevector[2] $\vec{k}_1 = n_1 k_0 (a\hat{x} + b\hat{z})$; one of these waves is the control field and the other is the probe field as defined in Sec. 2.1. I assume that the susceptibility for the control field is zero, so I can immediately use the Fresnel transmission coefficient given by Eq. (2.17b) and Snell's law to determine both amplitude and wavevector of the control field

---

[2] If I ignore residual Doppler broadening, the fact that the control field's wavevector is different in magnitude from the probe field's is irrelevant.

inside the vapour

$$\Omega_c(\vec{r}) = \Omega_c \exp(ik_0(\alpha x + \beta z)) \tag{2.20}$$

where $\alpha = n_1 \sin\theta = n_1 a$ and $\beta = \sqrt{1-\alpha^2}$. The susceptiblity for the probe field for a particular velocity class of atoms is

$$\chi(z, \vec{v}) = \frac{Nd^2}{\hbar\epsilon_0} \frac{\delta + i\gamma}{|\Omega_c \exp(ik_0\beta z)|^2 - (\delta + i\gamma)(\Delta_c - \vec{k}_3 \cdot \vec{v} + \delta + i\Gamma/2)} \tag{2.21}$$

where the only position dependence is on the z-coordinate. Often the spatial variation of the control field is not included in the susceptibility (such as in Eq. (2.8)), but in the case of selective reflection the spatial variation is of critical importance.

The incident probe field is described as an electric field $\vec{E}_1(\vec{r}) = \vec{E}_1 \exp(i\vec{k}_1 \cdot \vec{r})$, where $\vec{k}_1$ is defined as above. I assume that the polarization of the wave is solely in the $\hat{y}$ direction. I label the reflected and trasmitted probe fields as in Sec. 2.2. From the boundary condition given in Eq. (2.15b) and the form of the susceptibility in Eq. (2.21), I know that the x-dependence of the reflected and transmitted fields must be the same as that of the incident field: $e^{ik_0\alpha x}$. From Eq. (2.14), one can deduce that the reflected field must therefore be a plane wave of the form

$$\vec{E}_2(\vec{r}) = \vec{E}_2 \exp(in_1k_0(ax - bz)). \tag{2.22}$$

Since the probe susceptibility can depend on position the transmitted probe field will not always be a plane wave. In general, I cannot use the Fresnel equations to determine the amplitude of the reflected field. The problem is now to find the amplitude of the reflected probe field $\vec{E}_2$ given the above conditions, and the additional assumption that the susceptibility of the atoms is small ($\chi \ll 1$).

2.4 Solution for incident angles below the critical angle

If the incident field intersects the interface at an angle that is less than the critical angle for total internal reflection, then both the control field and the probe field are travelling waves inside the atomic vapour. Their common wavevector is then simply $\vec{k}_3 = k_0(\alpha\hat{x} + \beta\hat{z})$, where β is a real quantity. The spatial dependence of the control field, as given in Eq. (2.20), is then purely a phase factor, and its magnitude does not vary with space. Therefore, the susceptibility in Eq. (2.21) does not vary with position, indicating that the EIT medium is *homogeneous*. That means that the machinery of the Fresnel equations can be used to calculate both the transmitted and reflected probe fields, as long as I use $n_2 = \sqrt{1+\chi}$. Nominally, the range of validity of this analysis is for all $\theta \leq \theta_c$.

There is a subtlety here that involves the motion of the atoms, as they are not allowed to roam around all of space. There is an interface with which they can collide, and this can have a significant impact on the reflection coefficient. This analysis has been done in detail for two-level atoms by Nienhuis *et al.* [24], and I freely admit that much of the theory in this thesis was based on their work. I will describe the general principle of how the motion of atoms can affect the reflection coefficient, and then I will state the conditions under which I can ignore it.

Consider a gas of two level atoms with a ground state and an excited state. When an atom collides with the wall it loses all coherence, and its state reverts to that of the ground state. One must then distinguish between atoms that are approaching the surface and have yet to collide, and atoms that have already collided and are leaving the surface. Atoms that are approaching the surface are assumed to have had an infinity of time to approach, so they must be in the steady state by the time they reach the surface. It is the transient behaviour of the atoms that leave the surface after being de-excited that causes a measurable change in the reflection spectra. In the limit of no saturation one can show that the contribution of atoms leaving the surface is exactly the same as those that are approaching the surface, so that to correctly account for the motion of the atoms one must integrate the susceptibility over **half** the Maxwell velocity distribution in the z-direction. For angles that are far from the critical angle, this has a profound impact on the two-level absorption spectra. In the case of near normal incidence this will result in a lopsided Doppler profile, and for angles near grazing incidence this results in profiles that are narrowed compared to their Doppler counterparts.

The magnitude of this transient effect depends on the magnitude of the z-component of the transmitted wavevector, be it real or imaginary. For angles near the critical angle, the z-component of the transmitted wavevector is much smaller than that of the x-component of the wavevector. Therefore, the Doppler broadening associated with the x-direction washes out the transient effects of the collisions with the interface. In this thesis, I only investigate angles that are near the critical angle because they are the only angles that give a significant signal. Therefore, I ignore the effect of the transient behaviour of the atoms in my calculation of the susceptibility. I account for the motion of the atoms by assuming the only wavevector component of interest for Doppler broadening is $\vec{k}_3 \cdot \hat{x} = k_0\alpha$, and I use Eq. (2.8) with the appropriate spatial variation of the control field. The factor Γ' then becomes $\Gamma' = \Gamma + 2\sqrt{2}\alpha k_0 v_T$.

The reflectivity of the interface is plotted for $\theta \leq \theta_c$ in Fig. 2.4. One notices that well below the critical angle, there is no distinct transmission peak as one would expect for EIT. In fact, it looks more like a dispersive resonance than a transmissive one. There are two ways of

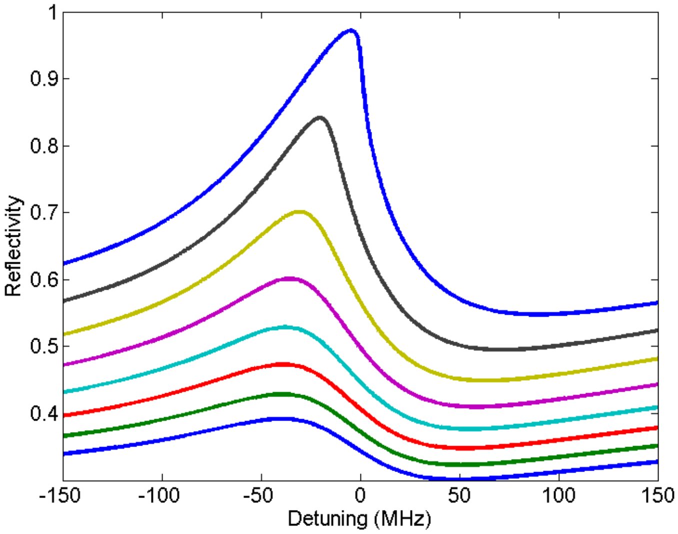

Figure 2.4: Theoretical plots of the reflectivity of the interface when $\theta < \theta_c$. The top curve corresponds to $\theta = \theta_c$, with the angular step for each curve being 2.2 mrad. The plots here are for $\Gamma = 2\pi \times 500$ MHz, $\Omega_c = 2\pi \times 100$ MHz, and $\gamma = 2\pi \times 1$ MHz.

understanding this: one is purely mathematical and the other intuitive. First, the mathematical reason. If one takes the Fresnel reflection coefficient r as defined in Eq. (2.17a) and expands it to first order in the susceptibility, one arrives at

$$r \approx r_0 \left(1 - \frac{n_1 \cos\theta}{n_1^2 - 1} \frac{\chi}{\beta} \right) \tag{2.23}$$

where I have defined $r_0 = r(n_2 = 1)$. For any complex variable z where $|z| \ll 1$, the quantity $|1+z|^2 \approx 1 + 2\Re(z)$ if we neglect second-order and higher terms. In Eq. (2.23) the appropriate complex variable is χ/β, and in the case of β being real the correction to the reflectivity is proportional to the real part of the susceptibility with a minus sign out front. This is why the spectra in Fig. 2.4 look very similar to the real part of the EIT susceptibility in Fig. 2.2.

The intuitive explanation is best done with the plot in Fig. 2.5. Recall that the critical angle is given by $\theta_c = \sin^{-1}(n_2/n_1)$, so that when n_2 increases the critical angle increases and vice-versa. In the case that n_2 describes an EIT medium, the index of refraction is lower for negative detunings and higher for positive detunings. This means that for negative detunings the critical angle is shifted to lower values and consequently the reflectivity increases. For positive detunings, the critical angle is shifted to higher values and the reflectivity decreases.

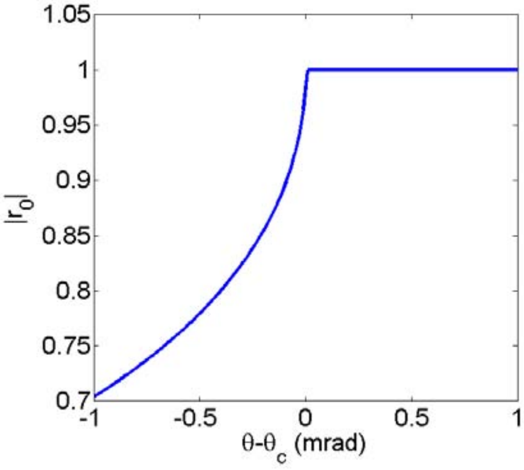

Figure 2.5: Magnitude of the reflection coefficient r_0 near the critical angle.

This dependence on the real part of the index of refraction is what leads to the dispersive spectra seen in Fig. 2.4.

2.5 Evanescent EIT

When the incident angle exceeds the critical angle, one unfortunately cannot use the Fresnel equations to calculate the reflection coefficient. The z-component of the transmitted wavevector, $k_0\beta$, is imaginary, and this means that the magnitude of the control field varies with the penetration depth z. Ergo, the medium is no longer homogeneous, and the Fresnel equations no longer apply. One must backtrack to the wave equation in order to solve this problem. Fortunately, there are many simplifications, both rigourous and approximate, that one can use to make this problem tractable.

Let us consider the wave equations (2.13) and (2.14). The reader may recall that I dispensed with the term $\nabla(\nabla \cdot \vec{P}(\vec{r}))$, and I did this by noting that $\nabla \cdot \vec{D}$ is equivalent to $\nabla \cdot \vec{E}$ when χ is independent of $\vec{r}$. At first glance, it would seem that I can no longer neglect this term. However, if the field is a plane wave whose polarization is solely in the $\hat{y}$ direction and propagates in the $x - z$ plane, then this term still vanishes when χ is a function of z only. Equation (2.14) still holds in the region $z > 0$.

I can further simplify the wave equation for this particular problem by noting that because the susceptibility is a function of z only, it cannot modify the properties of the wave in the x-direction. This follows from Eq. (2.15a). Since the incident field is a plane wave and varies along x as $e^{ik_0\alpha x}$, so too must the transmitted wave vary in the same manner. Let $\vec{E}_3(\vec{r}) = u_3(z)e^{ik_0\alpha x}\hat{y}$ and similarly for $\vec{E}_1$ and $\vec{E}_2$: the problem is to solve

$$(\partial_z^2 - k_0^2\eta^2)u_3(z) = -k_0^2\chi(z)u_3(z) \tag{2.24}$$

for the region $z > 0$ ($\eta = -i\beta = \sqrt{n_1^2 \sin^2\theta - 1}$) and the boundary conditions

$$u_1(0) + u_2(0) = u_3(0) \tag{2.25a}$$

$$\partial_z \left[u_1(z) + u_2(z)\right]|_{z=0} = \partial_z u_3(z)|_{z=0} \tag{2.25b}$$

where Eq. (2.25b) comes from Eq. (2.15c) and the relationship between $\vec{B}$ and $\vec{E}$. The above equations are as simple as I can make the problem, and unfortunately it is not simple enough. Equation (2.24) describes a wave-like entity travelling in the z-direction with a spatially varying wavevector. No analytical solution or solution method exists for the general problem, because if it did we would all know how to solve the Schrodinger equation exactly in one dimension for any potential. It is here that I must resort to approximation.

The key approximation that I shall use is the Born approximation which may be familiar to readers interested in scattering theory in quantum mechanics [42]. For the problem at hand, the physical content of the approximation is as follows: I assume that the transmitted wave is not substantially altered by the presence of the EIT medium. Let us imagine that there are no atoms for a moment and consider the transmitted electric field. We know that this is a field which decays exponentially into the vapour, and its amplitude is given by the Fresnel equations. Now re-introduce the atoms. The vacuum expression for the transmitted electric field induces a particular polarization on the atoms, which in turn generates an electric field that propagates both towards the interface and away from the interface. Now, the polarization of the atoms is determined not just by the external field (the vacuum expression for the transmitted field), but by the **total** field. So the field that is produced by the atoms must be added to the external field, and thus the polarization of the atoms must be recalculated. With the new polarization, we get a different electric field, and so it goes *ad infinitum*. The only way to calculate this infinite progression self-consistently is to solve Eq. (2.24) exactly. The first order Born approximation cuts this progression off at the first term: I calculate the electric field produced by the atoms if their polarization is determined by the vacuum expression for the transmitted field. I do not consider the back-action of the atoms on themselves.

With that long-winded explanation out of the way, let us return to a mathematical description. I write that the transmitted field is given as the sum of a zeroth and first order term $u_3(z) = u_3^{(0)}(z) + u_3^{(1)}(z)$ and similarly for the reflected field $u_2(z)$. The zeroth order term solves the pair of differential equations

$$\begin{aligned} &(\partial_z^2 - k_0^2\eta^2)u_3^{(0)}(z) = 0 \qquad z > 0 \\ &(\partial_z^2 + n_1^2 k_0^2 b^2)u_2^{(0)}(z) = 0 \quad z < 0 \end{aligned} \tag{2.26}$$

subject to the boundary conditions given in Eqs. (2.25a) and (2.25b) with each $u_i(z)$ replaced with $u_i^{(0)}(z)$. Thus, the zeroth order terms are nothing but the solutions in the case of no atoms: travelling or evanescent waves where the amplitudes at $z = 0$ are related by Fresnel equations.

The first order terms solve the differential equations

$$\begin{aligned} &(\partial_z^2 - k_0^2\eta^2)u_3^{(1)}(z) = -k_0^2\chi(z)u_3^{(0)}(z) \quad z > 0 \\ &(\partial_z^2 + n_1^2 k_0^2 b^2)u_2^{(1)}(z) = 0 \qquad\qquad\qquad\quad z < 0 \end{aligned} \tag{2.27}$$

subject to the boundary conditions

$$u_2^{(1)}(0) = u_3^{(1)}(0) \tag{2.28a}$$

$$\partial_z u_2^{(1)}(z)|_{z=0} = \partial_z u_3^{(1)}(z)|_{z=0}. \tag{2.28b}$$

The solution for the region $z < 0$ is simple: it is a travelling wave. But the solution for the region $z > 0$ is not as simple, although it is possible to obtain analytically. The use of the Green's function method for solving this problem is the subject of the next section.

2.6 Green's functions for evanescent EIT

The method of Green's functions that I use in this section borrows heavily from Tai [43]. The problem that I want to solve is now

$$\begin{aligned} &(\partial_z^2 - k_0^2\eta^2)g_3(z|z') = -\delta(z - z') \quad z > 0 \\ &(\partial_z^2 + n_1^2 k_0^2 b^2)g_2(z|z') = 0 \qquad\qquad z < 0 \end{aligned} \tag{2.29}$$

subject to the boundary conditions

$$g_2(0|z') = g_3(0|z') \tag{2.30a}$$

$$\partial_z g_2(z|z')|_{z=0} = \partial_z g_3(z|z')|_{z=0} \tag{2.30b}$$

for the Green's functions $g_3(z|z')$ and $g_2(z|z')$. The Green's functions must satisfy several conditions: they must be continuous at $z = z'$, the derivative of $g_3(z|z')$ must change at $z = z'$ by -1 and they must be symmetric with respect to exchange of z and z'. This is, of course, in addition to satisfying the differential equations for $z \neq z'$ and the relevant boundary conditions. One can construct the Green's function for the region $z > 0$ as the sum of two terms: one from the point source polarization $\delta(z - z')$ and the other from the wave scattered from the interface. For the region $z < 0$, we only need the scattering term as there is no polarization in that region. The coefficients of the scattering terms are chosen so that the boundary conditions are satisfied. Thus, the Green's function for the region $z > 0$ is

$$g_3(z|z') = \frac{1}{2k_0\eta} \begin{cases} e^{-k_0\eta(z-z')} + r' e^{-k_0\eta(z+z')} & z \geq z' \\ e^{k_0\eta(z-z')} + r' e^{-k_0\eta(z+z')} & 0 \leq z \leq z' \end{cases} \tag{2.31}$$

and the Green's function for the region $z < 0$ is

$$g_2(z|z') = \frac{1}{2k_0\eta} t' e^{-in_1k_0bz - k_0\eta z'} \tag{2.32}$$

where $r' = \frac{i\eta - n_1b}{n_1b + i\eta}$ and $t' = \frac{2i\eta}{n_1b + i\eta}$ are the reflection and transmission coefficients as seen from the EIT medium. The first order correction to the transmitted field is then the convolution of the Green's function $g_3(z|z')$ and the polarization

$$u_3^{(1)}(z) = -k_0^2 \int_0^\infty \chi(z') t u_1^{(0)}(z') g_3(z|z') dz'. \tag{2.33}$$

To determine $u_2^{(1)}(z)$, we use Eq. (2.28a) and the fact that the reflected field is a travelling wave. This means that $u_2^{(1)}(z) = u_3^{(1)}(0) \exp(-in_1k_0bz)$. One can show that this is equivalent to convolving the polarization with the Green's function given in Eq. (2.32). The first order correction to the reflected field is thus

$$\begin{aligned} u_2^{(1)}(0) &= \frac{k_0}{2\eta}\left(\frac{2n_1 b}{n_1 b + i\eta}\right)\left(\frac{2i\eta}{n_1 b + i\eta}\right) u_1^{(0)}(0)\int_0^\infty \chi(z')e^{-2k_0\eta z'}dz' \\ &= u_1^{(0)}(0) r_0 \frac{2ik_0 n_1 b}{(n_1^2-1)}\int_0^\infty \chi(z')e^{-2k_0\eta z'}dz' \end{aligned} \tag{2.34}$$

where I have included the transmission of the incident field into the vapour (first set of brackets in first line) and the transmission of the field from the vapour into the dielectric (second set of brackets). Equation (2.34) bears striking resemblance to the second term in Eq. (2.23); so much so in fact, that I am motivated to introduce the effective susceptibility

$$\chi_{\text{eff}} = 2k_0\eta \int_0^\infty \chi(z')e^{-2k_0\eta z'}dz' \tag{2.35}$$

$$= \frac{Nd^2\sqrt{\pi}}{\hbar\epsilon_0}\frac{\delta + i\gamma}{\Omega_c^2}\log\left(1 - \frac{\Omega_c^2}{(\delta+i\gamma)(\delta+\Delta_c+i\Gamma'/2)}\right) \tag{2.36}$$

where the last line is obtained from a straightforward (seriously!) integration. The effective susceptibility can then be used directly in Eq. (2.23).

A plot of the reflectivity of the interface above the critical angle is shown in Fig. 2.6. Two plots are shown: one (blue) using Eq. (2.36), and the other (red dashed) ignores the variation of control field with depth. One can see that the lineshape, properly described using the variation of the control field, is distinctly non-Lorentzian. The intuitive reason is this: since the width of the transparency window is determined by the intensity of the control field, atoms that are close to the interface will see a much wider transparency window than those that are farther away. The farthest atoms will see a transmission window whose width is limited by the ground state dephasing rate. The sum of all the Lorentzians with different widths results in the distinctive lineshape. I have plotted the effective susceptibility for only one angle in Fig. 2.6, as the theory predicts no variation of the shape with angle.

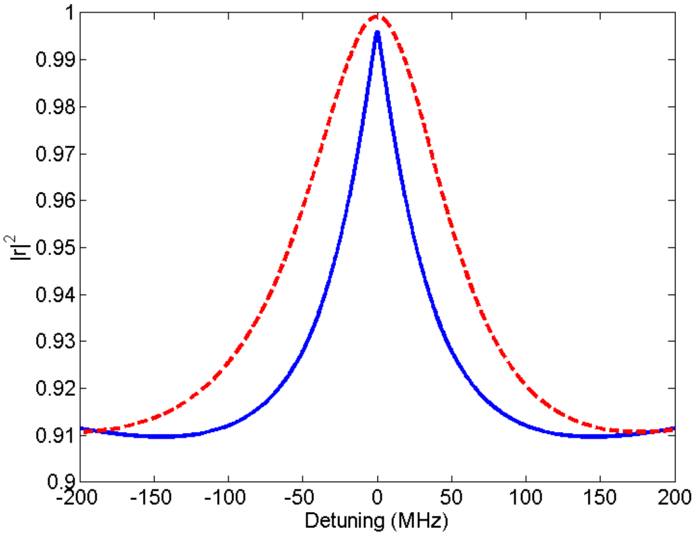

Figure 2.6: Reflectivity of the interface for $\theta = \theta_c + 3^\circ$. The solid blue curve uses the effective susceptibility as given by Eq. (2.36) whereas the red dashed curve uses the regular EIT susceptibility given by Eq. (2.8).

2.7 Limitations

Every model has its limitations, and the one described in the preceding pages is no exception. There are two main limitations to the model. The first is that, assuming incident plane waves, it is not valid for incident angles near the critical angle. Near the critical angle the first order correction to the reflected field blows up, rendering the model unphysical. Further, one can intuitively see that the variation in the real part of the index of refraction near the critical angle will lead to the transmitted probe field sometimes being a travelling wave, sometimes an evanescent wave, depending on the detuning. This will lead to hybridization of the lineshapes near the critical angle. The second, related, limitation is that I assume that we have incident plane waves. In most experiments, and in particular ours, both the control and the probe field are Gaussian beams which can be decomposed into a sum of plane waves. Therefore, they have a finite range of incident angles, and near the critical angle some angles can experience TIR and some will not. This can also lead to hybridization of the line shape. All that being said, I would like to discuss in the following sections possible corrections and improvements to the model that could be used if higher precision was desired.

2.7.1 Higher order Born approximation

It is reasonably straightforward to formally extend the derivation of the correction to the reflected field in Sec. 2.6 to higher order terms in the Born approximation. To do so, I write that the z-dependent part of the transmitted field is

$$u_3(z) = \sum_{n=0}^{\infty} u_3^{(n)}(z) \tag{2.37}$$

and similarly for the reflected field. Each order n then solves the differential equations

$$\begin{aligned} (\partial_z^2 - k_0^2\eta^2)u_3^{(n)}(z) &= -k_0^2\chi(z)u_3^{(n-1)} \quad && z > 0 \\ (\partial_z^2 + n_1^2k_0^2b^2)u_2^{(n)}(z) &= 0 && z < 0 \end{aligned} \tag{2.38}$$

with the appropriate boundary conditions relating the transmitted and reflected fields of the same order. In Eq. (2.38), $u_3^{(n)}(z) = 0$ for $n < 0$. The unfortunate problem with this extension is that to calculate each new correction of order n to the reflected field I have to have already calculated the profile of the transmitted field to order $n - 1$. The formal solution for the transmitted field $u_3^{(1)}$ is given by Eq. (2.33). All subsequent orders for the polarization will have the same form, except with $u_3^{(0)}(z)$ replaced with $u_3^{(n-1)}(z)$. From the boundary conditions we always know what the reflected field is. So the formal solution for the n^{th} order correction to the reflected field is the following equation:

$$u_2^{(n)}(0) = k_0^{2n} \int_0^\infty dz_1 \int_0^\infty dz_2 \ldots \int_0^\infty dz_n \chi(z_1)g_3(0|z_1)\chi(z_2)g_3(z_1|z_2)\ldots\chi(z_n)g_3(z_{n-1}|z_n)u_3^{(0)}(z). \tag{2.39}$$

As it turns out, the calculation for the first order correction to the transmitted field can be done analytically. However, the resulting expression conveys no real physics, and the expression for the reflected field cannot be computed analytically. Instead, I will simply plot the results with the second order correction in Fig. 2.7. I would like to draw attention to the fact

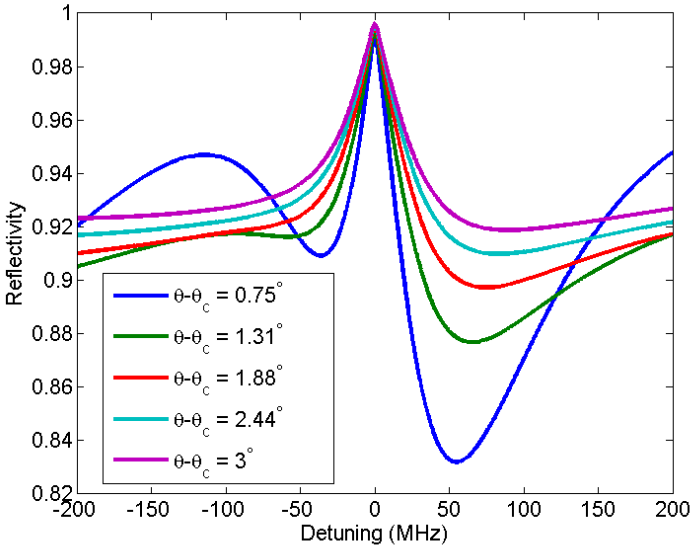

Figure 2.7: Theoretical reflectivity of the interface as a function of detuning for $\theta_c + 0.75^\circ \leq \theta \leq \theta_c + 3^\circ$ when the second order correction is included.

that while the first order correction does not introduce asymmetry in the reflectivity as a function of angle, the second order correction clearly does. This is likely because while the zeroth order transmitted field is independent of the detuning, the first order transmitted field is not. The polarization that it produces will generate a reflected field that is certainly not symmetric about zero detuning.

I would like to point out that in Fig. 2.7 I have purposely included traces that show large deviations from the traces corresponding to larger angles. The experimental data do not show this kind of structure, but it is unclear as to why not. Perhaps the fact that we have Gaussian beams washes out such structure near the critical angle, or perhaps higher orders of the Born approximation are required.

2.7.2 Gaussian Beams

In all of the above work, I have assumed that I have infinite plane waves and thus only one wavevector to work with. What about the case where both the probe and the control field are beams of finite size and therefore with some spread in wavevectors? This section will develop a simple model that accounts for a finite spread in wavevectors using the machinery developed in the previous sections. Further details about the Gaussian beams at interfaces can be found in Kozaki *et al.* [44].

Consider the coordinate system shown in Fig. 2.8. Starting with the 'incident coordinates',

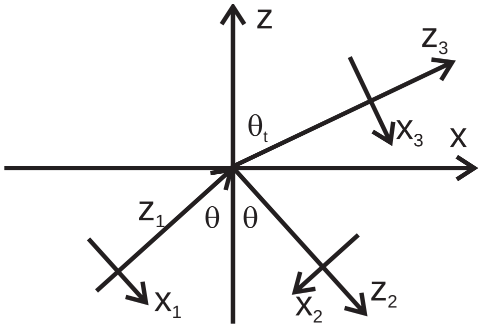

Figure 2.8: Coordinate system used for considering the transformation of a Gaussian beam at an interface. The incident coordinates are (x_1, z_1), the reflected coordinates are (x_2, z_2), and the transmitted coordinates are (x_3, z_3). The coordinates (x, z) are the interface coordinates. The origin of the z coordinate for the incident, reflected and transmitted systems is at the origin of the interface coordinates.

I know from the Fourier transformation of the Helmholtz equation that, given an initial distribution of wavevectors $E_1(k_{x_1}, 0)$, the propagating field is

$$E_1(x_1, z_1) = \frac{1}{2\pi}\int_{-\infty}^{\infty} E_1(k_{x_1}, 0)\exp(iz_1\sqrt{n_1^2k_0^2 - k_{x_1}^2} + ik_{x_1}x_1)dk_{x_1}. \tag{2.40}$$

I use a standard coordinate transformation between the incident and interface coordinates to find that the incident field at the $z = 0$ plane is given by

$$E_1(x, 0) = \frac{1}{2\pi}\int_{-\infty}^{\infty} E_1(k_{x_1}, 0)\exp(ip(k_{x_1})x)dk_{x_1} \tag{2.41}$$

where $p(k_{x_1}) = k_{x_1}\cos\theta + \sin\theta\sqrt{n_1^2k_0^2 - k_{x_1}^2} \approx k_{x_1}\cos\theta + n_1k_0\sin\theta$ is the projection of the wavevector along the interface coordinate x in the paraxial approximation. Now, I want to determine what the spatial profile of the transmitted field is. To do so, I again use the solution for the Helmholtz equation given an initial distribution of wavevectors

$$E_3(x,z) = \frac{1}{2\pi}\int_{-\infty}^{\infty} E_3(p,0)\exp(iz\sqrt{k_0^2 - p^2} + ipx)dp \tag{2.42}$$

where the distribution $E_3(p,0)$ can be determined from Eq. (2.41) and the Fresnel transmission coefficient t (Eq. (2.17b)). Note that $\cos\theta = \sqrt{n_1^2k_0^2 - p^2}/(n_1k_0)$ and $\cos\theta_t = \sqrt{k_0^2 - p^2}/k_0$. Additionally, I have made the approximation that $\chi \ll 1$ so that I may ignore the effect of the atoms on the wavevectors. After playing around with integrals and delta functions and worrying about 2π's, the final expression for the transmitted field is

$$E_3(x,z) = \frac{1}{2\pi}\int_{-\infty}^{\infty} t(p(k_{x_1}))E_1(k_{x_1},0)\exp(iz\sqrt{k_0^2 - p(k_{x_1})^2} + ip(k_{x_1})x)dk_{x_1}. \tag{2.43}$$

All I need to do is apply the above equation to the control and the probe fields to calculate what the correction to the reflection coefficient is. However, there is a bit of a snag. In my derivation of Eq. (2.34) I assumed that the only x-dependence was a phase factor. That is no longer the case, so I must make a further approximation. If I ignore the spatial variation of the control field, then the susceptibility is still independent of x and the only spatial variation in x is a simple phase factor. Further, I will also ignore the x variation of the probe field outside of the phase factor, as it contributes little to the underlying physics. These two approximations allow me to use the Green's functions derived in Sec. 2.6 and also significantly reduce the mathematical complexity.

Addressing the Green's functions themselves, I would like to point out that the derivation of the Green's functions relied in no way on the fact that they were decaying exponentials. In general they are of the form $e^{ik_0\beta z}$, where β can be complex. At first glance, it appears that the integral in Eq. (2.35) will not converge if β is solely real. However, β can never be solely real because it is defined through $k_0\beta = \sqrt{k_0^2 - p(k_{x_1})^2}$, and $p(k_{x_1})$ extends over an infinite range for most fields that can be generated in the lab. Therefore, I claim that the integral always converges.

After all those arguments, I finally want to actually write down an expression for the reflected field. Under the first order Born approximation, the reflected field for an incident plane wave with transverse wavevector k_{x_1} is

$$E_2(k_{x_1}, 0) = r_0(k_{x_1})E_1(k_{x_1}, 0) + \frac{2in_1k_0}{n_1^2 - 1} r_0(k_{x_1})E_1(k_{x_1}, 0)b(k_{x_1}) \int_0^\infty \chi(z)e^{2ik_0\beta(k_{x_1})z}dz \tag{2.44}$$

where one must remember that the position dependence of χ is due to the control field having the form given in Eq. (2.43). To get the total reflected field, I simply integrate over the initial distribution:

$$\begin{aligned} E_2(0) = \int_{-\infty}^{\infty} E_2(k_{x_1}, 0)dk_{x_1} &= \int_{-\infty}^{\infty} r_0(k_{x_1})E_1(k_{x_1}, 0)dk_{x_1} \\ &+ \frac{2in_1k_0}{n_1^2 - 1} \int_{-\infty}^{\infty}\int_0^{\infty} r_0(k_{x_1})E_1(k_{x_1}, 0)b(k_{x_1})\chi(z)e^{2ik_0\beta(k_{x_1})z}dzdk_{x_1}. \end{aligned} \tag{2.45}$$

As one might imagine, the above equation cannot be integrated analytically, so I have plotted the reflection spectrum in Fig. 2.9. The important feature to note is that the model using Gaussian beams does not show the same divergence when the angle of incidence is slightly above the critical angle as compared to the plane wave case. The amplitude of the EIT signal

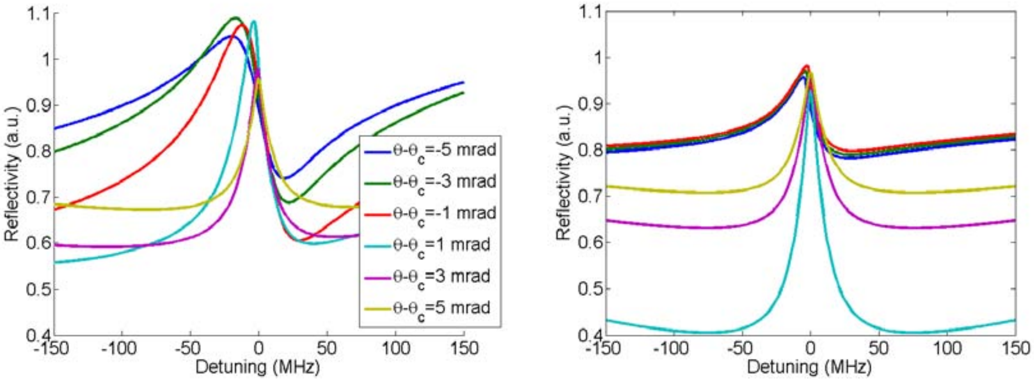

(a) Reflectivity assuming a Gaussian probe beam with angular divergence of 0.5 mrad. (b) Reflectivity assuming a plane wave probe field.

Figure 2.9: Reflectivity of the interface for both Gaussian and plane wave probe fields. Curves of the same colour correspond to the same angle between the two graphs.

saturates at a finite value. This allows us to see that the lineshape should change smoothly between a dispersive signal to a sharp transmission peak. Note, however, that the Gaussian beam model has its own problems, such as the reflectivity being larger than unity near the critical angle. The reason is that I have still invoked the first-order Born approximation before inserting finite-sized beams, and that procedure will never be valid near the critical angle. Effectively what I have done is to smooth out the singularity at θ_c for beams of non-zero divergence, but the singularity remains if the divergence approaches zero. On physical grounds there should be no singularity for plane waves, so this naive model still remains incorrect near the critical angle.

2.8 Goos-Hänchen shift

The Goos-Hänchen shift (GHS) was first proposed in 1929 by Picht [45] and first measured by F. Goos and H. Hänchen in 1947 [26]. The basic idea is that if a light beam is totally internally reflected it picks up a phase that depends on the angle of incidence. This angle-dependent phase can be represented as a wavevector dependent phase $e^{i\phi(\vec{k})}$. For a beam with a small spread in wavevectors, I can approximate $\phi(\vec{k}) \approx \phi_0 + \frac{d\phi}{dk_{x_1}} k_{x_1}$ where k_{x_1} is the transverse wavevector. The reflected beam in the reflected coordinates (see Fig. 2.8) is then

$$E_2(x_2, 0) = \frac{1}{2\pi} \int_{-\infty}^{\infty} E_2(k_{x_1}, 0) \exp(ik_{x_1} x_2 + i\phi_0 + i\frac{d\phi}{dk_{x_1}} k_{x_1}) dk_{x_1} = E_2(x_2 - \frac{d\phi}{dk_{x_1}}, 0) \quad (2.46)$$

where a property of Fourier transforms leads to a shift in the position of the beam. Therefore, the point on the interface that the reflected beam appears to originate from is not the same as that expected from geometrical optics as shown in Fig. 2.10. There are two ways to visualize the GHS by considering that it relies on evanescent fields. The first is to imagine that the beam is reflecting not off of the interface but off of the skin layer a distance $(k_0\sqrt{n_1^2 \sin^2\theta - n_2^2})^{-1}$ into the rarer medium. The second way to visualize it is to consider that in evanescent fields energy flows parallel to the interface, not perpendicular to it. Therefore, the energy of the beam

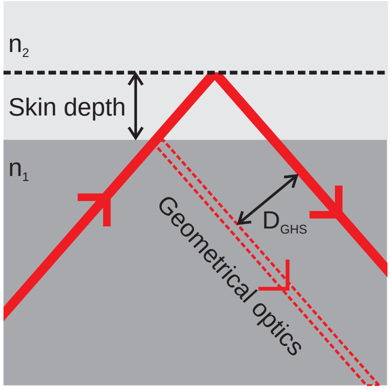

Figure 2.10: Diagram of the GHS. The actual reflected beam (solid) appears to come from a different location on the interface compared to the expectation from geometrical optics (dashed). One possible interpretation of the shift is that the beam reflects off of the skin layer created by the evanescent field.

flows parallel to the interface for a short distance before re-emerging [46].

The mathematical derivation starts from the reflection coefficient given in Eq. (2.17a). When $\theta > \theta_c$, the magnitude of the reflection coefficient is unity, but the phase varies with the incident angle. The phase imparted to a totally reflected beam with polarization perpendicular to the plane of incidence is

$$\phi = 2\tan^{-1}\left(\frac{\sqrt{\sin^2\theta - \frac{n_2^2}{n_1^2}}}{\cos\theta}\right). \tag{2.47}$$

I take the derivative of the above equation with respect to θ, and using $\frac{d}{dk_{x_1}} \approx \frac{1}{k_0}\frac{d}{d\theta}$ I find that the GHS is [47]

$$D_{GHS} = \frac{1}{k_0}\frac{d\phi}{d\theta} = \frac{1}{k_0}\frac{2n_1\sin\theta}{\sqrt{n_1^2\sin^2\theta - n_2^2}}. \tag{2.48}$$

Apparently one can get a giant lateral displacement by sending in a beam at an angle arbitrarily close to the critical angle. This is obviously unphysical, and this problem persists in every derivation of the GHS starting from plane waves. It is possible to derive an expression valid near the critical angle if one uses a Gaussian ansatz [48], and this derivation shows that the maximum displacement will always be much less than the beam width. Therefore, from single reflection experiments it is impossible to achieve a giant GHS. That being said, it is possible to achieve large displacements if one uses multiple reflections as in the original experiment [26].

In addition to the lateral GHS, there is also an angular Goos-Hänchen shift (AGHS). This phenomena was originally proposed by Ra *et al.* [49] in 1977 and measured by Merano *et al.* [27] in 2009. The AGHS is exactly what its name suggests: the beam is reflected at an angle that is different from the geometrical optics expectation as shown in Fig. 2.11. Therefore, the angle of incidence is not equal to the angle of reflection. In contrast to the lateral GHS, the AGHS occurs only when there is partial reflection of the incident field. In a sense it is easier to understand: an angle-dependent amplitude change causes the beam to reshape and therefore the beam's center-of-mass shifts in k-space.

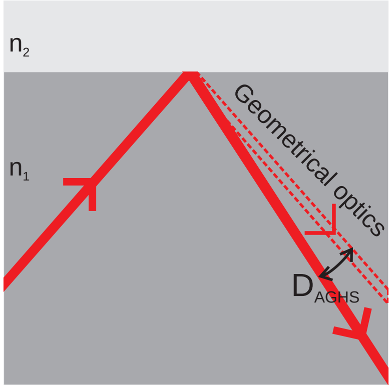

Figure 2.11: Diagram of the AGHS. An incident beam is reflected at an angle that is different than the angle of incidence.

To derive the AGHS, I will assume that I have an incident Gaussian beam of waist w_0 whose Fourier transform is $E(k_{x_1}, 0) = \exp(-k_{x_1}^2 w_0^2/4)$. The reflected field, in the reflected coordinates as defined in Fig. 2.8, is

$$E_2(x_2, 0) \approx \frac{1}{2\pi} \int_{-\infty}^{\infty} r(k_{x_1}) \exp\left(-\frac{k_{x_1}^2 w_0^2}{4} + i k_{x_1} x_2\right) dk_{x_1}. \tag{2.49}$$

Let us write $r = \exp(\log r)$. If I approximate $\log r \approx \log r|_{k_{x_1}=0} + \frac{d \log r}{dk_{x_1}}|_{k_{x_1}=0} k_{x_1}$, then the integrand is a product of a Gaussian and an exponential. Thus, the argument of the Gaussian undergoes the transformation $k_{x_1}^2 w_0^2/4 \rightarrow \frac{w_0^2}{4}(k_{x_1} - \frac{2}{w_0^2}\frac{d \log r}{dk_{x_1}})^2$. The actual angular shift is then

$D_{\text{AGHS}} = \frac{2}{k_0^2 w_0^2}\frac{d\log r}{d\theta}$. Grinding through the derivatives, I find that the angular shift is

$$D_{AGHS} = \frac{2}{k_0^2 w_0^2}\frac{2n_1 \sin\theta}{\sqrt{n_2^2 - n_1^2 \sin^2\theta}}. \tag{2.50}$$

Note that the angular shift is inversely proportional to the square of the beam waist: this suggests that for small beams the angular shift can become quite large. However, this expression likely has the same limitations as Eq. (2.48), as it derives from the same underlying assumptions, so the angular shift cannot exceed the beam divergence. In general, one can write down the expression for both the lateral and the angular GHS as the real and imaginary parts of the derivative of the logarithm of the reflection coefficient [50]

$$iD_{GHS} + k_0 w_0^2 D_{AGHS} = \tilde{D} = \frac{1}{k_0}\frac{d\log r}{d\theta}. \tag{2.51}$$

This form is especially useful when calculating the modification to the GHS caused by the presence of an EIT medium. Given the reflection coefficient in Eq. (2.23), where depending on the regime I will use the regular or the effective susceptibility, the GHS is given by

$$\tilde{D} = \tilde{D}(\chi = 0) - \frac{n_1 \sin\theta}{k_0 \beta^3}\chi - \frac{n_1 \cos\theta}{k_0 \beta (n_1^2 - 1)}\frac{\partial \chi}{\partial \theta}. \tag{2.52}$$

The above equation hides some very interesting physics. All resonant media will have the second term, where the GHS is modified by the frequency-dependent change in the index of refraction of the medium. Atomic vapours will also have the third term in the case of linear absorption because the Doppler broadening of the medium will change slightly with a change in the incident angle. But in an atomic vapour under EIT conditions, the third term can be very large. The reason is that in order to get EIT in an atomic vapour, one needs the wavevectors for the probe and control fields to be parallel (phase-matched). Recall from Sec. 2.1 that in order to account for Doppler broadening I replace $\Delta_c \to \Delta_c - \vec{k}_c \cdot \vec{v}$ and $\delta \to \delta - (\vec{k}_p - \vec{k}_c) \cdot \vec{v}$ and then integrate over a Maxwell distribution of velocities. An angular misalignment of the two fields by an angle $\delta\theta$ results in additional Doppler broadening on the order of $\delta\theta k_p v_T$ that adds directly to the ground-state dephasing γ. If this is comparable to or larger than the power broadened EIT linewidth (Eq. (2.9)) then the EIT window will be destroyed. This fact is known in regular atomic vapour cells where the Doppler broadening acts as a spatial filter for divergent beams [51, 52]. Therefore, to get EIT and hence an effect of EIT on the GHS we require that probe field have a divergence such that $\theta_{\text{div}} k_p v_T \ll \Omega_c^2/\Gamma'$. This is equivalent to requiring that the divergence be much less than the ratio of the EIT linewidth to the Doppler linewidth. For the case of an EIT linewidth of 1 MHz and a Doppler linewidth of 200 MHz this corresponds to a divergence of 5 mrad, or a 50 μm wide beam at a wavelength of 795 nm.

The sensitivity of the EIT effect to good alignment means that the index of refraction is very sensitive to changes in the angle of the probe beam. In the case of total internal reflection, the extreme sensitivity of the index of refraction to changes in angle corresponds to an extreme sensitivity of the reflected phase with respect to angle. This can translate into a giant GHS which is due *entirely to the motion of atoms inside the vapour*, unlike other proposals where giant beam shifts due to EIT are created from multiple reflections [53]. Interestingly, the faster the atoms move the larger the beam shift. Note that this conclusion is likely not subject to the same limitations as Eqs. (2.48) and (2.50), as I don't need to be near the critical angle.

To quantitatively show the giant GHS, I shall consider the case of EIT with evanescent fields, as that is traditionally where the lateral beam shift is expected, and I use the effective susceptibility as given in Eq. (2.36) to perform the calculation. The two places where the Doppler effect enters are the one-photon and EIT decoherence rates Γ' and γ'. As a reminder, the Doppler broadened one-photon linewidth under the condition of evanescent EIT is given as $\Gamma' = \Gamma + 2\sqrt{2} n_1 \sin\theta k_0 v_T$. In general, wavevector mismatch changes γ to $\gamma'(\theta)$. The wavevector mismatch in evanescent fields is

$$\Delta\vec{k}(\theta) \cdot \hat{x} = \Delta k(\theta) = n_1 k_0 (\sin\theta - \sin\theta_{\text{ctrl}}) + \Delta k \sin\theta_{\text{ctrl}} \tag{2.53}$$

where θ_{ctrl} is the angle of incidence of the control field, and Δk is the wavevector mismatch for parallel fields. Usually, one wants $\theta_{\text{ctrl}} = \theta$, but in order to correctly describe the modification to the GHS I will keep the angles separate for now. At the end of the calculation I shall set them equal to each other. Exactly how the decoherence rate is modified due to wavevector mismatch depends on the details of the system, for which I will give two examples below.

It is straightforward to show that

$$\begin{aligned}\frac{\partial\chi}{\partial\theta} &= \frac{\partial\Gamma'}{\partial\theta}\frac{\partial\chi}{\partial\Gamma'} + \frac{\partial\gamma'}{\partial\theta}\frac{\partial\chi}{\partial\gamma'} \\ &= 2\sqrt{2}n_1k_0v_T\cos\theta\frac{\partial\chi}{\partial\Gamma'} + \frac{\partial\gamma'}{\partial\theta}\frac{\partial\chi}{\partial\gamma'} \end{aligned} \tag{2.54}$$

where

$$\frac{\partial\chi}{\partial\Gamma'} = \frac{iNd^2\sqrt{\pi}}{2\hbar\epsilon_0}\frac{\delta + i\gamma'}{(\delta + i\Gamma'/2)[(\delta + i\gamma')(\Delta_c + \delta + i\Gamma'/2) - \Omega_c^2]} \tag{2.55}$$

and

$$\frac{\partial\chi}{\partial\gamma'} = \frac{iNd^2\sqrt{\pi}}{\hbar\epsilon_0}\left(\frac{1}{\Omega_c^2}\log\left(1 - \frac{\Omega_c^2}{(\delta + i\gamma')(\Delta_c + \delta + i\Gamma'/2)}\right) + \frac{i}{(\delta + i\gamma')(\Delta_c + \delta + i\Gamma'/2) - \Omega_c^2}\right), \tag{2.56}$$

and I evaluate the two above equations at $\theta_{\text{control}} = \theta$. I admit that the preceding expressions are not very transparent, but they do show some qualitative features. Note that both equations approach zero for $\delta = 0$ as $\Omega_c \to \infty$, so there is no giant GHS if I drive the atoms very hard. On the other hand, if $\Omega_c \to 0$ Eq. (2.56) also approaches zero. Therefore, to get a maximum enhancement of the GHS I have to set the control field to some intermediate value where the sensitivity of the EIT window to decoherence is maximized. They also show that the modification to the beam shift due to Doppler broadening of the natural line is very small: it scales roughly as Γ'^{-2} in Eq. (2.55). Compare this with the second term in Eq. (2.52) due to modification of the index of refraction which scales as Γ'^{-1}. Thus, we do not expect a large change in the beam shift due to the one-photon Doppler effect.

Now I want to find how the particular decoherence mechanism affects the GHS. For ballistic atoms with average thermal velocity v_T, the decoherence rate is modified by simple Doppler broadening to become

$$\gamma' = \gamma + \sqrt{2}\Delta k(\theta) v_T \tag{2.57a}$$

$$\frac{\partial \gamma'}{\partial \theta} = \sqrt{2} n_1 k_0 v_T \cos\theta. \tag{2.57b}$$

So the decoherence rate for ballistic atoms scales linearly with the Doppler broadening, and the modification to the GHS scales as Γ'^0. In Fig. 2.12 I plot the spectrum of the GHS in the case of ballistic atoms. Clearly, there is a significant enhancement of both the lateral and the angular beam shifts near the EIT window, and these occur when the control field Rabi frequency satisfies $\Omega_c^2/\Gamma\gamma \approx 1$. The maximum lateral beam shift occurs at the points where the real part of the susceptibility is maximized, while the the maximum angular shift occurs when the imaginary part is maximized. The reason is that the lateral shift is due to a phase change with angle, and that depends on the real part of the susceptibility. The angular shift

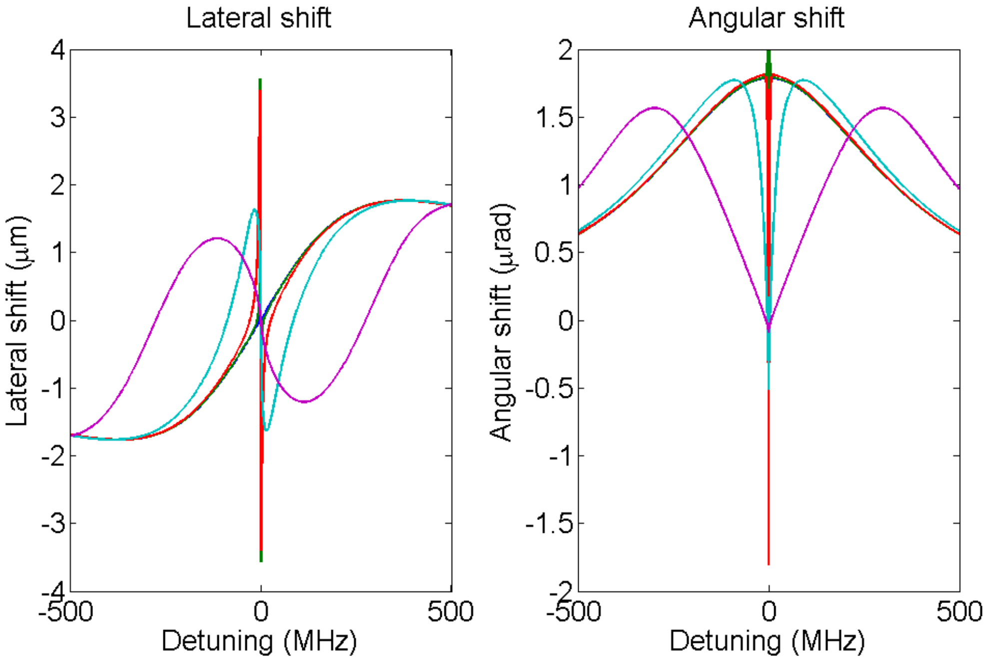

Figure 2.12: Beam shift calculated from Eq. (2.52) for ballistic atoms. The angle was set to be 5 mrad above critical, the ground state decoherence to be $2\pi \times 0.5$ MHz, the ground-excited state decoherence rate to be $\Gamma = 2\pi \times 5.6$ MHz, the temperature to be $T = 180$°C, and the beam waist to be 500 μm. Each curve is for a different control field power logarithmically spaced from $\Omega_c = \sqrt{10^2\Gamma\gamma}$ (purple) to $\Omega_c = \sqrt{10^{-2}\Gamma\gamma}$ MHz (blue).

depends on an amplitude change with angle, and this is related to the imaginary part. Note that if I considered the case when the incident angle is below the critical angle the opposite argument would hold. Note also that if the atoms are moving ballistically, then there is no extra collisional broadening of the line which is why $\Gamma = 2\pi \times 5.6$ MHz in Fig. 2.12

If I have atoms that move diffusively, rather than ballistically, then the modification to the decoherence mechanism has a quadratic dependence on the wavevector [51] given by

$$\gamma' = \gamma + D\Delta k(\theta)^2 \tag{2.58a}$$

$$\frac{\partial \gamma'}{\partial \theta} = 2n_1 D\Delta k k_0 \cos\theta \tag{2.58b}$$

where D is the diffusion coefficient. One way to think about this case compared to ballistic atoms is that the diffusing atoms move with an effective thermal velocity $D\Delta k$, which is much less than v_T. This results in a much smaller modification to the GHS, as can be clearly seen in Fig. 2.13 Contrary to the case of ballistic atoms, the beam shifts increase monotonically over

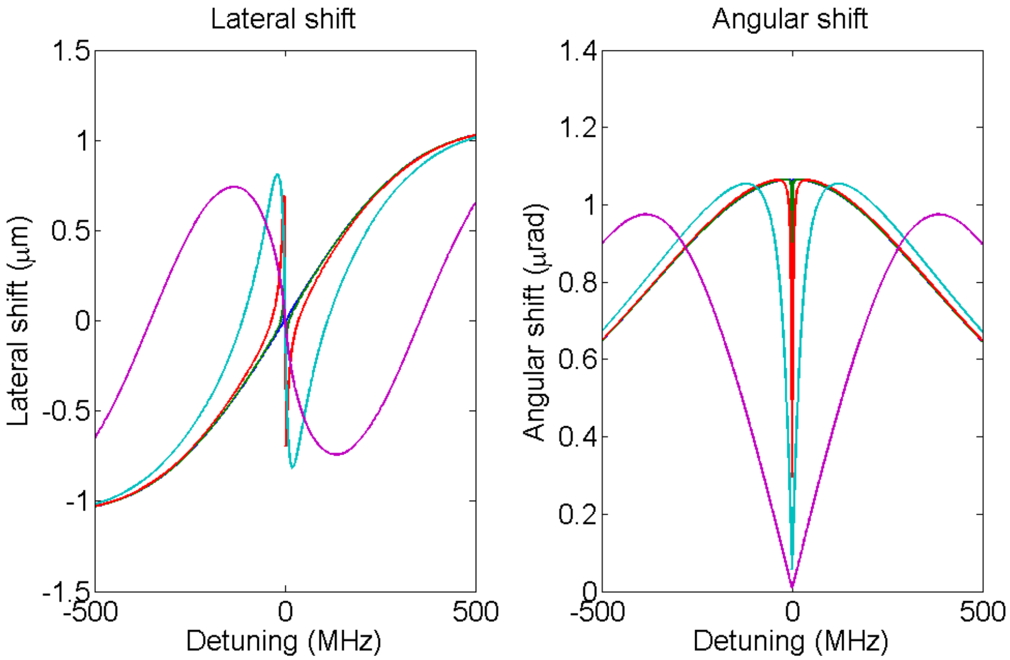

Figure 2.13: Beam shift calculated from Eq. (2.52) for diffusive atoms. The parameters are the same as in Fig. 2.12, except here the diffusion coefficient is set to be 5 cm^2/s and $\Gamma = 2\pi \times 505.6$ MHz. due to collisional broadening.

the range of control field powers in Fig. 2.13. The monotonic increase is because the third term in Eq. (2.52) is much less than the second term which depends only on χ, and χ increases with Ω_c over a much larger range. To more clearly illustrate the difference between the diffusive and ballistic regimes, I show the maximum beam shifts as a function of control field Rabi frequency in Fig. 2.14. There is clearly a peak in the maximum shift obtained with ballistic atoms near $\Omega_c^2/\Gamma\gamma \approx 1$ that is absent in the case of diffusive atoms. The maximum shift also increases with decreasing bare decoherence γ. Unfortunately, neither shift in Fig. 2.14 is large enough to fully separate two beams that could experience EIT – the condition for the entire beam to experience EIT being that its width is much large than 50 μm. While one could imagine decreasing the decoherence rate further there is a lower limit imposed by the residual Doppler

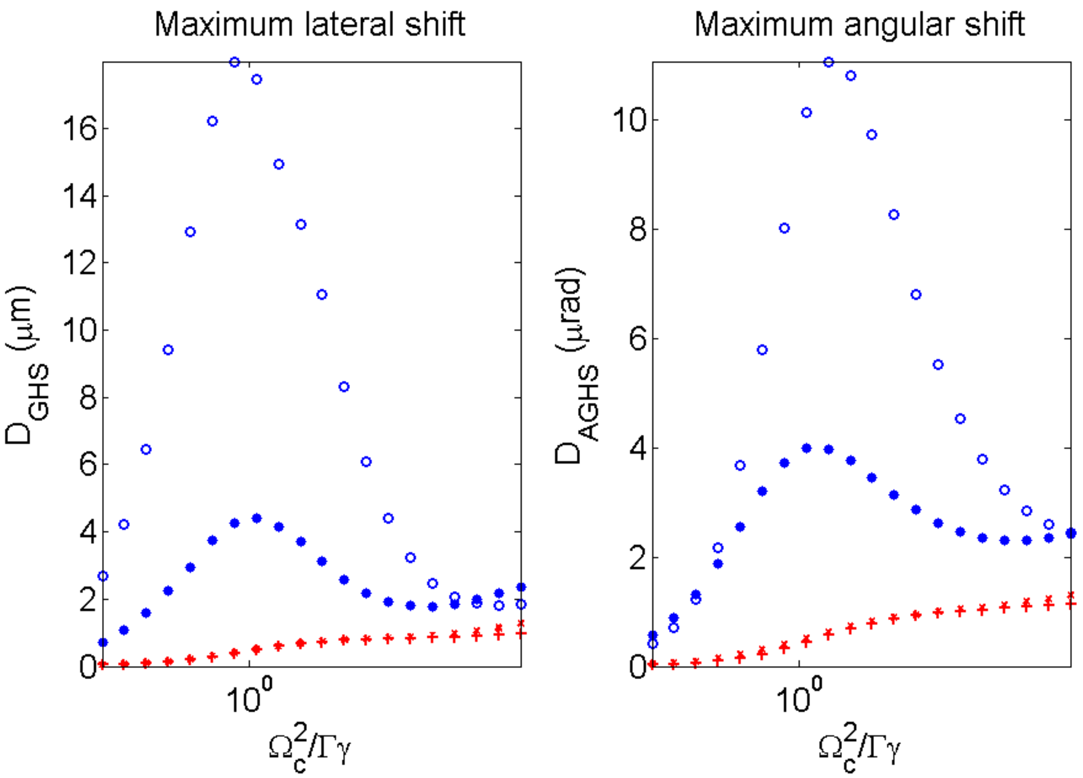

Figure 2.14: Maximum beam shifts for ballistic (blue) and diffusive (red) atoms. The bare decoherence is $\gamma = 2\pi \times 0.5$ MHz for the blue solid circles and red x's, while $\gamma = 2\pi \times 0.1$ MHz for the blue open circles and red +'s. Other parameters are the same as in Fig. 2.12

.

broadening for parallel beams of $\gamma \approx 2\pi \times 5$ kHz. Therefore, to further increase the beam shifts one would need to increase the temperature of the cell and thus the number density, with the goal of achieving a lateral beam shift larger than the beam width or an angular beam shift larger than the beam divergence (for this example, $\theta_{\text{div}} \approx 500\ \mu$rad). With a large enough beam shift, the enhanced GHS could be used as a frequency-selective beam separator.

Chapter 3

Experiment

In this chapter, I will discuss the actual experimental apparatus used to detect evanescent EIT. The purpose of this section is to provide enough detail to re-create this particular experiment based almost entirely on this chapter and the references therein.

The reader may notice that the first person pronoun partially changes from the ‘I’ of the previous section to the ‘we’ of the subsequent sections. I have done so because while the theoretical section was almost entirely my work, the actual experiment was performed with significant assistance from others. It therefore seems rather arrogant to continue to exclusively use the singular pronoun.

3.1 Atomic System

Our atomic system is rubidium-87. Rubidium is a convenient atomic medium for our purposes for several reasons. The first is that, as an akali metal, it has one free valence electron and hence a simple electronic structure. As a result, all of its spectroscopic properties have been well investigated both theoretically and experimentally [54]. A second reason is that, as an akali metal, it has a high vapour pressure even at room temperature. In regular EIT experiments, it is therefore easy to obtain high optical depths at moderate temperatures. In our case, it is possible to obtain very large number densities at high but still reasonable temperatures. Lastly, the transition wavelengths in rubidium are at convenient wavelengths in the near infrared, where both cheap laser diodes and high-quality Titanium-Sapphire lasers exist.

The lowest lying optical transitions in ^{87}Rb are the D1 and D2 transitions, and these have central wavelengths of 794.978 nm and 780.241 nm, respectively. We use the D1 transition as our approximation to a Λ-level system. The energy level diagram for that particular transition is shown in Fig. 3.1. The D1 transition is convenient for our purposes because the hyperfine splitting of all the levels of interest are large enough that it is possible to resolve individual transitions in a Doppler broadened gas without resorting to more complex spectroscopic techniques. In particular, the upper hyperfine splitting is about 800 MHz which is larger than the Doppler broadened width of the individual transitions.

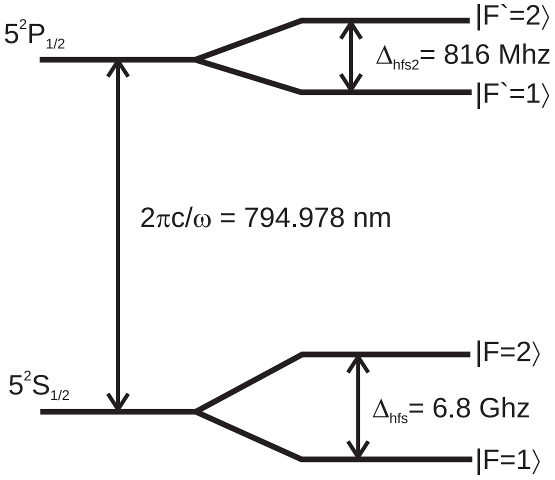

Figure 3.1: Level diagram for the D1 transition in ^{87}Rb .

In our experiment we use the $|F = 1\rangle \rightarrow |F' = 1\rangle$ transition as the probe transition and the $|F = 2\rangle \rightarrow |F' = 1\rangle$ as the control field transition. The large hyperfine splitting between the two ground states is convenient because it means that we can ignore the problem of the control field also coupling to the probe transition. This effectively means that we can use large control field Rabi frequencies, as the condition for ignoring the coupling is that $\Omega_c \ll \Delta_{\text{hfs}}$, where Δ_{hfs} is the hyperfine splitting. The large hyperfine splitting is one reason we use ^{87}Rb instead of the more abundant ^{85}Rb, which has a hyperfine splitting of about half that of ^{87}Rb .

3.2 Optical setup

An overview of the optical apparatus is shown in Fig. 3.2. We generate a probe field from a

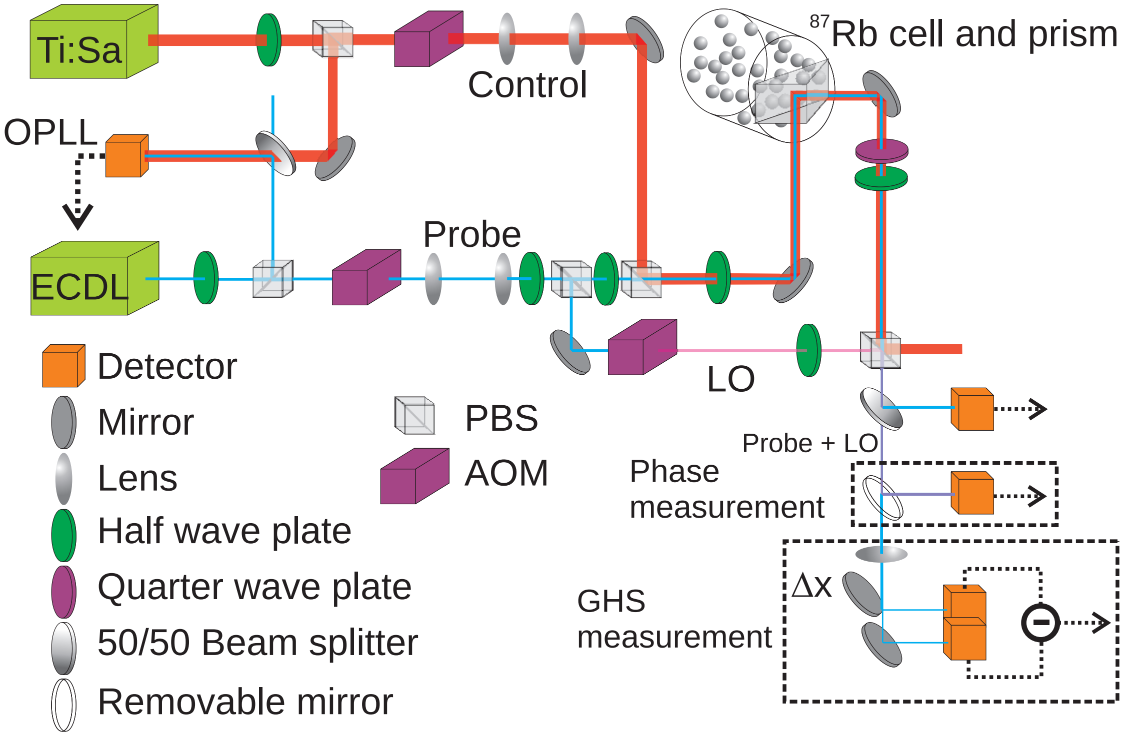

Figure 3.2: Diagram of setup. PBS stands for a polarizing beam-splitting cube, AOM for acousto-optic modulator, and the mirror with a Δx represents a moveable mirror. The optical phase-locked loop (OPLL) is used to stabilize the frequency difference between the two lasers. LO is the local oscillator used for phase measurements, and is only present for those measurements. See text for remaining details.

home-built external-cavity diode laser (ECDL) [55] and a control field from a Coherent MBR-110 Ti:Sapphire (Ti:Sa) laser. The Ti:Sa acts as the master-oscillator as it has very good long-term and short-term stability. The short-term stability is achieved partly through the design of the laser cavity as a single monolithic block, and the laser has a short-term linewidth of less than 100 kHz. The long-term stability of the Ti:Sa is achieved via locking the laser cavity to a temperature-stabilized reference cavity inside the laser enclosure. In our experience, the Ti:Sa frequency does not drift by measurable amounts; it only makes rare large frequency hops which are easily detectable.

The ECDL has a short-term linewidth of about 1 MHz, and it lacks the long-term stability of the Ti:Sa. Since in EIT experiments one can achieve spectral features that can be considerably less than 1 MHz in width, a method for improving the ECDL linewidth is needed. Improved long-term stability is also desirable. We lock the frequency of the ECDL to the Ti:Sa using an optical phase-locked loop (OPLL). The procedure is as follows. First, we split off 2.5 mW of power from each laser and overlap the beams on an ultra-fast photodiode (New Focus 1577A, bandwidth of about 7 GHz). The photodiode is AC-coupled, so the signal that is measured is a sinuisoidal signal that oscillates at the frequency difference between the two lasers. For EIT, we need this frequency difference to be equal to the hyperfine splitting. We generate a signal at a frequency of about 18 MHz that is used as a seed for an electronic phase-locked loop that generates a signal at around 213 MHz. We can scan the frequency of the probe field by scanning the frequency of the 18 MHz signal over a small range. The 213 MHz signal and an amplified optical beat-frequency signal are sent to a phase-frequency detector (PFD) which digitizes the analog signals and divides them down to lower frequencies before digitally comparing the phase. The PFD generates an error signal which is separated into high- and low-frequency components which are sent to the ECDL's current and piezo modulation, respectively. This system allows us to obtain a relative linewidth between the probe and the control fields on the 1 Hz scale. The long-term stability of the ECDL is also much improved, as it is referenced the stability of the Ti:Sa. Further details about the OPLL can be found in [55, 56].

Aside from the small amount of power diverted for the OPLL, both the control and probe fields are sent through acousto-optic modulators (AOM) to enable pulsing of the fields for certain measurements. The measurements that require pulsed fields are measuring the phase profile of the reflected probe beam (Sec. 3.4), measuring the group delay (Sec. 4.4), and attempting storage of the probe field (not described in detail in this thesis, but see [55] for procedural details). The fields are continuous wave for the majority of measurements that we perform in the lab. The fields are then resized using telescopes; the probe field has a waist of about 0.5 mm, while the control field has a waist of about 1 mm. It is desirable for the control field to be larger than the probe field to reduce the effects of population exchange on the EIT profile [38]. The probe and control fields are combined on a polarizing-beam splitting cube (PBS) with opposite polarizations, and the polarization of the fields is rotated by 90° before the fields strike the cell. The polarization of the probe field at the cell is vertical in the lab frame (perpendicular to the plane of incidence). Since the two fields are nominally orthogonally polarized after the cell, we filter the control field using a combination of waveplates and a PBS. The reflected power in the probe is measured using a photodiode. Generally we can reduce the control field power that leaks through the polarization filtration optics down to about 30 μW – about a fifth of the power of the probe after the polarization filtration. Descriptions of the phase and GHS measurement sections in Fig. 3.2 will follow in subsequent sections.

3.3 Housing the atoms

Housing the atoms has to address four main issues associated with evanescent EIT. The first is how to generate the evanescent fields. The second is that we need to have a number density high enough that we can obtain a measurable EIT signal. Thirdly is that we have to minimize decoherence mechanisms. Finally, we have to be able to change the angle of incidence of the beams with enough precision that we can sweep over the critical angle and observe EIT signatures. The housing for the atoms that we designed meets all of these needs.

We use vapour cells containing isotopically pure ^{87}Rb with anti-reflection coated windows as our means of containing the vapour. In our experiment anti-reflection coated windows are unnecessary, and perhaps even detrimental, but they are the only type of cells available in our lab. Unfortunately at our operating temperatures the anti-reflection coating degrades, and over time it develops opaque patches. These patches adversely affect the EIT signals and our ability to use polarization filtration to eliminate the control field. The cells contain, in addition to rubidium, between 30-50 Torr of neon buffer gas depending on the cell. We use buffer gas to ensure that the atoms remain in the interaction region for as long as possible. With the inclusion of buffer gas the atoms move diffusively rather than ballistically, and they spend a much greater time inside the interaction region.

We generate evanescent fields using a right-angle prism that is mechanically clamped to one of the cell windows. In order to reduce losses at the interface we coat the the prism face and cell window with index-matching gel. Light that is incident on the prism face is refracted towards the normal, and this allows us to access angles both above and below the critical angle. The relevant angles are shown in Fig. 3.3. Given an incident angle θ_1, the angle that the ray makes with the prism/vapour (n_1/n_2) interface is $\theta = \pi/4 - \sin^{-1}(\sin\theta_1/n_1)$. This is important, as small changes in the incident angle result in changes in the prism/vapour angle that are a factor of $1/n_1$ less. Also useful is to calculate the critical angle for the ray incident on the prism which for $n_1 = 1.5$ (BK7 prism) is about $4.8°$.

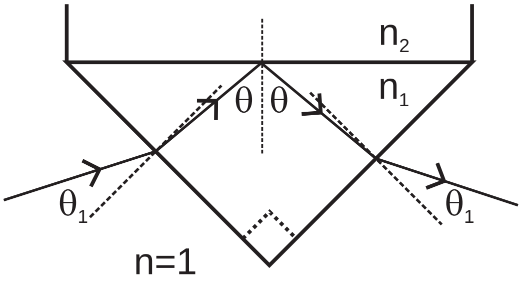

Figure 3.3: Ray diagram for reflection using a prism.

The cell is held in a cylindrical aluminum shell with the prism and cell window exposed so we can access them with the lasers. To reduce decoherence, the shell is enclosed in a mu-metal sleeve that is about twice as long as the aluminum shell. The purpose of the mu-metal sleeve is to eliminate static and low-frequency magnetic fields that may break the degeneracy of the magnetic Zeeman levels in ^{87}Rb and cause a reduction in contrast and broadening of the EIT line. The sleeve has slots cut into it so that the lasers can still access the prism and cell. The entire oven system can then be heated up to a measured temperature of about $130°$C, but with the addition of some standard house insulation the measured temperature can reach up to $200°$C. I am careful to specify "measured" temperature here, because the measured temperature is different from the temperature of the interface. The interface extends outside of the oven by about 1 cm, and is therefore colder than the actual oven. A detrimental effect of this extension is that rubidium condensation tends to form on the cell window, and this can adversely affect the measured EIT signals. For fine angular control, we mount the entire system on a New Focus 5-axis translation stage (model number 9081) which allows us to vary the angle of incidence with a stated precision of about 87 μrad.

As an interesting note, finding the critical angle for the first time was rather tricky. Later, we realized that it was made easier by the fact that the high number density of the atoms and the intense control field cause the atoms to fluoresce with purple light [57]. Measurements of the wavelength of the purple light by a colleague for a different experiment revealed that the fluorescent light is at 420 nm, which should be a distinctly blue colour. The only transitions in ^{87}Rb near 420 nm are the 6P to 5S transitions as shown in Fig. 3.4. Therefore, we conclude that

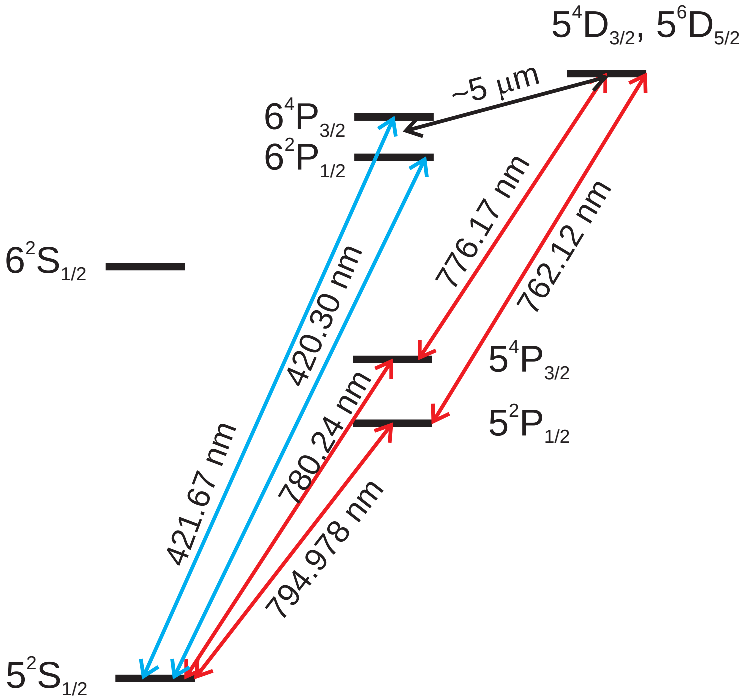

Figure 3.4: Extended rubidium-87 energy level scheme, neglecting the hyperfine levels [1]. The relevant allowed transitions for purple fluorescence are shown.

the fluorescent light is due to the decay of the atoms along that transition, and the purple colour is caused by mixing of the blue light with the strong red light scattered by the control field. The question now is how do the atoms reach states of such high energy under illumination from a field at 795 nm? Far off-resonant two-photon absorption of the 795 nm field is unlikely to be the cause because of the very large detunings. The most probable cause is an energy pooling process between two rubidium atoms that have been excited to the $5^2\mathrm{P}_{1/2}$ state [58]. In the energy pooling process, two excited rubidium atoms collide, and one atom is promoted to a higher energy state with nearly twice the energy of the original excited state, while the other atom is demoted to the ground state. The energy difference between the original excited state and the higher energy state is made up by a contribution from the kinetic energy of the atoms. Given the results of [58], our higher energy state is most likely one of the 5D states where the energy difference between an excitation directly from the 5S to 5D state and two excitations to the $5^2\mathrm{P}_{1/2}$ is

$$\Delta E = h(\nu_{\mathrm{5S}\to\mathrm{5D}} - 2\nu_{\mathrm{5S}\to 5^2\mathrm{P}_{1/2}}) = hc\left(\frac{1}{762.12\ \mathrm{nm}} - \frac{1}{794.978\ \mathrm{nm}}\right) \approx 67\ \mathrm{meV}.$$

In a gas at 105°C, corresponding to the approximate temperature of the interface (Sec. 4.2), approximately 40% of all atoms have thermal energy sufficient to bridge this energy gap. If an atom is promoted to one of the 5D states, it can radiatively decay to one of the 6P states by emitting a photon at approximately 5 μm [57], and then the atom can decay to the 5S state by emitting a 420 nm photon.

The purple fluorescence only occurs when the control field is a travelling wave inside the atoms, and hence it occurs only when the incident angle is less than the critical angle. Finding the critical angle is then a simple matter of adjusting the incident angle until the atoms stop fluorescing.

3.4 Phase Measurement

While measuring the reflectivity of the interface is done using a single photodiode, measuring the phase of the reflected signal poses some issues. One is how to measure it efficiently, preferably while scanning the frequency of the probe. Another is how to deal with phase fluctuations from mechanical noise on the optical table and from air currents created by the hot oven system. Our method for measuring the phase is to generate a LO from the probe field that is shifted in frequency by 110 MHz. The frequency shifting is done by an AOM as shown in Fig. 3.2. The LO is then combined with the probe field on the same PBS that filters the control field. The resulting beat-note is measured on a home-built photodetector with a 1 GHz bandwidth. The phase is measured by comparing the phase of the measured beat-note with the 110 MHz signal that drives the AOM using a phase-detector chip. The phase detector chip allows us to continually measure the phase difference while scanning the frequency of the probe field over the EIT resonance.

A further step is necessary to measure the phase as using RF interference signals does not eliminate the problem of mechanical noise and air currents which disturb the phase. The phase shift is also extremely small – on the order of tens of micro-radians. The scaling of the phase-detector chip is about 0.6 μV/μrad, which means that the voltage signal that we can measure is on the order of tens of micro-Volts. Our oscilloscope only has a sensitivity of a few milli-Volts. Furthermore, our interferometer has about a half-metre path length, so the voltages corresonding to phase fluctuations due to air currents and mechanical noise are large: around a Volt. We therefore use lock-in detection to amplify our signal while reducing the low frequency but large amplitude phase noise due to air currents.

Since lock-in detection is not necessarily a common technique, I will give a brief description of the principle behind it. Consider the case where one is measuring a signal $V(t)$ that is a combination of some desired signal $S(t)$ and some noise $N(t)$ where $V(t) = S(t) + N(t)$.

The idea of lock-in detection is to introduce a fast modulation to only the signal, so that the signal is shifted to a frequency sideband that is larger than the bandwidth of the noise. In our experiment we introduce an amplitude modulation, so the signal undergoes the transformation $S(t) \to (1 + A\sin(\omega_{\text{mod}}t))S(t)$ where ω_{mod} is the modulation frequency and A is the modulation depth. One then measures the total signal $V(t)$ and mixes it with a signal at the modulation frequency

$$\begin{aligned}\sin(\omega_{\text{mod}}t + \varphi)V(t) &= \sin(\omega_{\text{mod}}t + \varphi)(1 + A\sin(\omega_{\text{mod}}t))S(t) + \sin(\omega_{\text{mod}}t + \varphi)N(t) \\ &= \frac{A}{2}S(t)\cos\varphi + (S(t) + N(t))\sin(\omega_{\text{mod}}t + \varphi) - \frac{A}{2}\sin(2\omega_{\text{mod}}t + \varphi)S(t).\end{aligned} \tag{3.1}$$

One then uses a high-pass filter to eliminate all frequency components that are at ν_{mod} or higher. This eliminates all the noise $N(t)$ and leaves just the DC component which is proportional to $S(t)\cos\varphi$. By setting $\varphi = 0$, one gets a signal that is a scaled replica of the desired signal. Note that it is important to choose the filter and modulation frequencies appropriately; the modulation frequency not only has to be much larger than the noise bandwidth, it also has to be larger than the signal bandwidth so that one can choose a filter frequency that does not detrimentally affect the signal.

In the context of the model described above, our time-dependent signal is the phase shift on the reflected field due to EIT, and it varies in time as we scan the frequency of the probe field. The noise is due to air currents and mechanical noise. Since we are only interested in the phase fluctuations due to EIT, we modulate the amplitude of our signal by turning the control field on and off. This turns the EIT interaction on and off, but does not affect the noise due to air currents and mechanical instability. The square wave is not a sinusoidal modulation as described in the theory above, but the higher harmonics of the square wave do not contribute to the signal generated by the lock-in amplifier. During the mixing process all harmonics that have frequencies higher than ν_{mod} will be mixed to frequencies no lower than ν_{mod}; these then get eliminated by the high-pass filter.

The lock-in detector also amplifies the signal after it has been mixed and filtered, so it is necessary to calibrate the signal produced by the lock-in detector given a measured voltage. We do this by producing a signal with a known modulation at a larger voltage, and we measure the output of the lock-in as a function of the input voltage. This gives a calibration curve which can then be scaled to the different gain settings of the lock-in detector.

3.5 Beam shift measurement

The last aspect of the experiment was to measure both the lateral and angular GHS, and to do so we needed a way to measure the position of the beam. Other groups have used split-photodiodes [27] to measure beam shifts via power imbalances and then used a feedback loop to stabilize the beam to the center of the photodiode. The error signal provides a measure of the GHS. We do not have a split-photodiode, but we have the next best thing: a high-gain, low noise balanced detector originally used as a homodyne detector for quantum optics experiments. Our setup is then quite simple. We use the edge of a mirror to split the probe beam into two, and then we focus the resulting beams into the balanced detector. The mirror used to split the beam is mounted on a precision translation stage which allows us to adjust the mirror position in order to balance the detector.

In a simple model to determine how the signal is influenced by the beam position, let us assume that the signal V is related to the power in the left and right photodiodes by $V = g(P_L - P_R)$ where g is the photodiode gain. If we assume that the power in the left channel is $P_L = P_0(\frac{1}{2} + x)$ where P_0 is the total power in the beam and $-1/2 \leq x \leq 1/2$ is the beam position relative to center, then $V = 2gP_0x$. Thus, the signal is proportional to the product of the total power and the displacement of the beam. In order to accurately measure the GHS, one must also measure the reflectivity of the interface at the same time. This is why we use a $50/50$ beam splitter in our experiment as shown in Fig. 3.2.

The above model would apply only in the case of a square top-hat beam. For our beams, we have to take into account their Gaussian profile as well as possible asymmetric gains of the two photodiodes. Our signal is then $V = g_L P_L - g_R P_R$, and by conservation of energy[1] we have that

$$P_R = \frac{g_L P_0 - V}{g_L + g_R}. \tag{3.2}$$

If we cut a Gaussian beam of width w_0 with a straight edge, the power to the right of the edge will be

$$\begin{aligned} P_R &= \frac{2P_0}{\pi w_0^2} \int_{-\infty}^{\infty} dy' \int_x^{\infty} dx' e^{-2x'^2/w_0^2} e^{-2y'^2/w_0^2} \\ &= \frac{P_0}{2} \text{erfc}\left(\frac{\sqrt{2}x}{w_0}\right), \end{aligned} \tag{3.3}$$

so the relation of the beam deviation x to the measured signal is

$$x = \frac{w_0}{\sqrt{2}} \text{erfc}^{-1}\left(2\frac{g_L - V/P_0}{g_L + g_R}\right) \tag{3.4}$$

where $\text{erfc}(x) = \frac{2}{\sqrt{\pi}} \int_x^{\infty} e^{-x^2} dx$.

Finally, one can wonder how to differentiate between the lateral GHS and the angular GHS. In principle, one could simply look at the scaling of the beam shift as the distance between the interface and the detector increases. However, there is a simpler method for doing so. We place a lens in the path of the probe beam at such a location that an image of the interface is formed on the pick-off mirror. Since the image distance is defined as the distance from the lens such that all rays that start from the same point on the object end on the same point on the image, regardless of angle, the only beam shift that can be measured is the lateral beam shift. This also has the distinct advantage of eliminating a great deal of beam-pointing noise induced by the hot oven. The combined lateral and angular shift can be measured without the lens, and the two measurements (with and without) can be compared to determine the angular shift alone.

---

[1] Strictly speaking, conservation of energy *does not* imply conservation of power. In the case of a system which can store energy, the power entering the system does not necessarily have to be the power leaving the system. In our experiment, however, the mirror does not store energy, so conversation of energy *does* imply conservation of power.

Chapter 4

Results

The following sections will present our results regarding EIT spectra using selective reflection, as well as characterization of those spectra. Further theoretical discussion will be provided as warranted. Additionally, I will present our results on measurements of the GHS in the presence of an EIT medium.

4.1 EIT Spectra

The first issue I must address is whether or not we have measured a non-linear optical effect. That evidence is shown in Fig. 4.1 when the angle of incidence is 3 mrad above the critical angle. When the the probe is detuned far from resonance (curve (a)) the reflectivity is unity and does not change with frequency. If the probe field is tuned to resonance with the control field off, there is a reduction in the reflectivity of the interface as the probe field is absorbed by the atoms in the evanescent field. If the control field is turned on, then we observe a transmission peak at the two photon resonance (zero detuning). The increase in the baseline of the signal between curves (b) and (d) is due simply to the leakage of the control field through the polarization filtration optics. When we measured the signal that corresponds to the control field leakage and add it to the on-resonance curve (b), we find that the baselines of the two signals match (curve (c)).

The contrast of the EIT window is often important, especially in quantum memory experiments. The EIT contrast is defined as the ratio of the transmission peak amplitude to the probe absorption. In the case of Fig. 4.1, the measured contrast is about 36% for a moderate control field power. We have been able to achieve contrasts of over 40% with larger control field

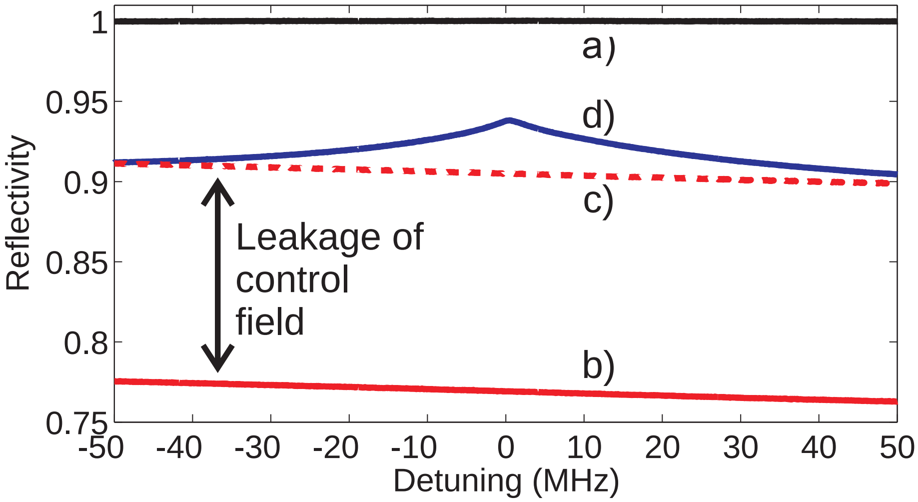

Figure 4.1: Reflectivity of the interface under various conditions. a) Probe field scanning far off-resonance, control field present. b) Probe field scanning over resonance, control field absent. c) Same as b), but the control field power that leaks through the filtering PBS is added to show consistency between a) and b). d) Probe field scanning over resonance, control field present. Control field power is 75 mW, and $\theta - \theta_c \approx 3$ mrad.

powers, although this necessarily leads to significant broadening of the EIT line.

We generally leave the control field on and measure the reflected probe power as a function of the detuning for different angles. Figure 4.2 shows two representations of the spectrum of the reflected probe field for a large range of angles. We see that the reflection spectra behave qualitatively similar to what was predicted in Chapter 2. For angles below the critical angle, we observe a dispersive lineshape whose amplitude grows as the angle increases. For angles much larger than the critical angle, the lineshape is a sharp transmission peak that shows similar structure to what was predicted in Sec. 2.6. We see that there is a broad pedestal with a narrow cusp feature at the two-photon resonance. Again, the amplitude of the transmission peak decreases as the angle is tuned away from the critical angle. Near the critical angle we see a smooth transition between the dispersive lineshape and the transmission peak.

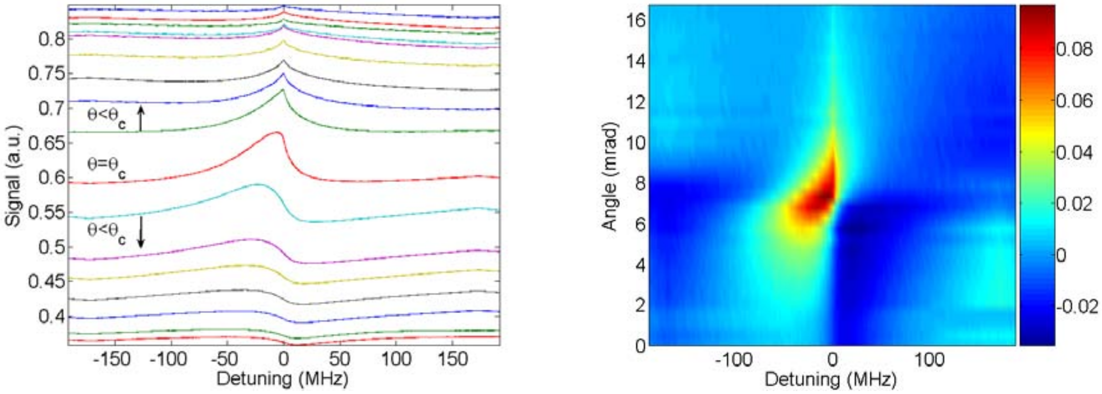

(a) Reflected probe power as a function of detuning. Each curve corresponds to a different angle, where the angular separation between each curve is about 0.52 mrad.

(b) Reflected probe power as a function of both angle and detuning. The colour scheme shows the signal as a relative deviation from the average value of each curve.

Figure 4.2: Two representations of the reflected probe power. The angular axis is not calibrated to the critical angle, and is simply to provide the correct relative angular scale but not an absolute scale.

4.2 Theoretical comparison

In order to quantitatively compare the theory developed in Chapter 2 with the data, we need to separate the data into regimes where $\theta < \theta_c$ and where $\theta > \theta_c$. For each regime, we then need to apply the appropriate model to the data. Figure 4.3 shows the result of that procedure. A few notes are in order so that I might meaningfully compare the theory to the data. First, we do not measure the absolute angular scale. It is possible to measure the angular scale in an absolute sense by determing where the beam strikes the entrance of the prism at 90° using the back-reflection of the beam. This provides an angular reference to which all other angle measurements can be related. The issue with that method is that it is insufficiently precise for our purposes. Our method for measuring the absolute scale is only accurate to about 0.18°, although we can measure the relative angle much more precisely. The difference in angle between each spectrum in Fig. 4.2 is $\sim 0.045^\circ$, and near the critical angle one can already see that the spectrum changes significantly from curve to curve. To the degree of precision afforded by our absolute measurement, we find that the traces that exhibit hybridization of the two lineshapes correspond to the angles near the critical angle. In order to proceed with theoretical comparisons, we therefore manually adjust the offset angle to achieve the best theoretical agreement. The angles used for each trace in the theoretical fits are then determined from this offset angle and our calibration of the angular scale.

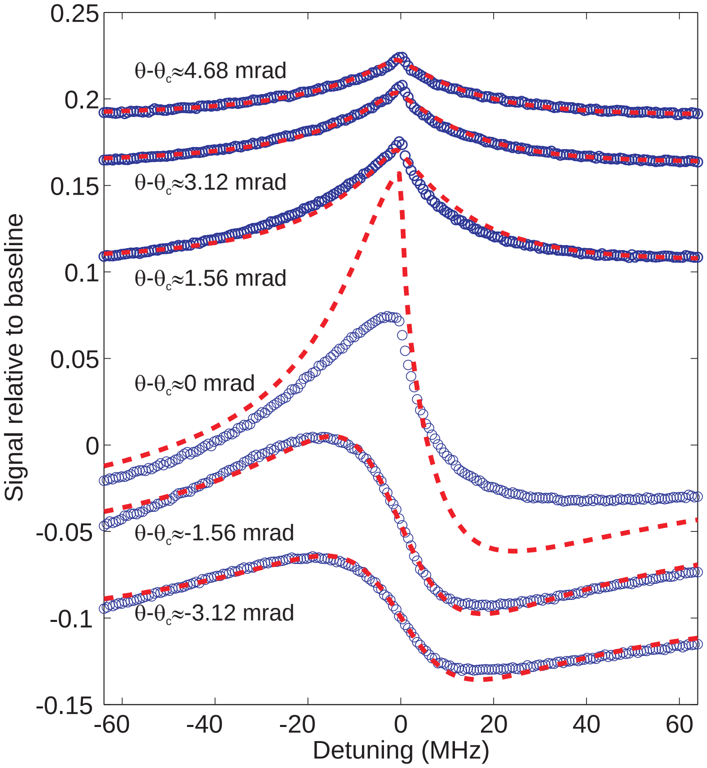

Figure 4.3: Reflection spectra for a range of angles extending below and above the critical angle. Blue circles are experimental data and red dashed lines are the theoretical fits. Each curve is calculated by taking the raw spectra, subtracting the mean and then dividing the result by the mean again to get a relative amplitude. Each trace here is offset by an arbitrary amount for illustrative purposes.

We allow only the offset to vary freely when fitting the theory to the data. We do this because there are several unknowns about the interface. The first is that the cell window is anti-reflection coated for 90° incidence, and we do not know its reflectivity as a function of incidence. The second reason is that the index matching gel used between the prism face and the cell window does not provide perfect matching between the two indicies of refraction. One can observe this in the lab by looking at the reflection of the strong control field off of the interface; one sees a triplet of beams emerging from the interface. In the case of perfect index matching, there should only be one reflected beam corresponding to the beam that is reflected from the window-vapour interface. The extra spots come from reflections from the prism-gel and gel-window interfaces. Therefore, imperfect index-matching contributes to our lack of knowledge about the interface reflectivity. Lastly, the cell window is not a perfectly clean and uniform surface. While we attempt to clean the exterior window of the cell and the prism face as well as possible, some dust or dirt will always remain. The interface also extends by about a centimeter outside of the oven, so the cell window is colder than the rest of the cell. This leads to condensation of rubidium on the window. If the lasers strike a spot with rubidium condensation, the observed EIT signal is significantly lower than when the fields strike bare glass. Problems arise when the condensation covers a considerable portion of the window, and one must compromise. An additional issue with the difference in temperature between the oven and the interface is that the atomic number density may be lower than predicted from the temperature alone. While we could measure the interface reflectivity *in situ* when the cell is cold, such a measurement would only be valid if nothing about the interface changed, such as the location and extent of the rubidium condensation.

The values of the control field Rabi frequency and atomic number density are allowed to change between the two different regimes of $\theta < \theta_c$ and $\theta > \theta_c$. For $\theta < \theta_c$, $\Omega_c = 2\pi \times 160$ MHz and $N = 6.8 \times 10^{18}$ m^{-3}, whereas for $\theta > \theta_c$ $\Omega_c = 2\pi \times 210$ MHz and $N = 6.0 \times 10^{18}$ m^{-3}. These number densities correspond to a temperature of approximately 105°C, correlating well with our observation that the interface temperature should be colder than the measured temperature of the oven. The small change in the number density between the two regimes is mildly puzzling, but not particularly worrisome as it is only on the order of 10%. The large change in Ω_c is worrisome, because it indicates that the EIT transmission peak is wider in the evanescent case than in the travelling wave case. Exactly why this is the case is not clear.

The ground state decoherence rate is fixed at $2\pi \times 0.5$ MHz in accordance with independent measurements (see Sec. 4.3.1), and the excited state linewidth is set by the sum of the natural linewidth of 5.6 MHz, the collisional broadening of approximately 500 MHz, and the Doppler broadening which varies slightly with angle.

We can clearly see from Fig. 4.3 that the theory is in reasonable agreement with the data for $\theta < \theta_c$ and for $\theta \gg \theta_c$. This is especially so for angles less than critical. At the critical angle the amplitude is far larger than expected, but this is not surprising because our theory is not valid at the critical angle. To evaluate more carefully the quality of the fit for angles greater than θ_c, we present a close up of the fit and data for the trace corresponding to $\theta - \theta_c \approx 4.68$ mrad in Fig. 4.4. A small discrepancy appears between theory and data at two-photon resonance where the cusp occurs. A possible reason for the discrepancy may be that we have neglected atomic diffusion into and out of the interaction region. Diffusion will appear several times later in the thesis, so it is prudent to pause here and elaborate further.

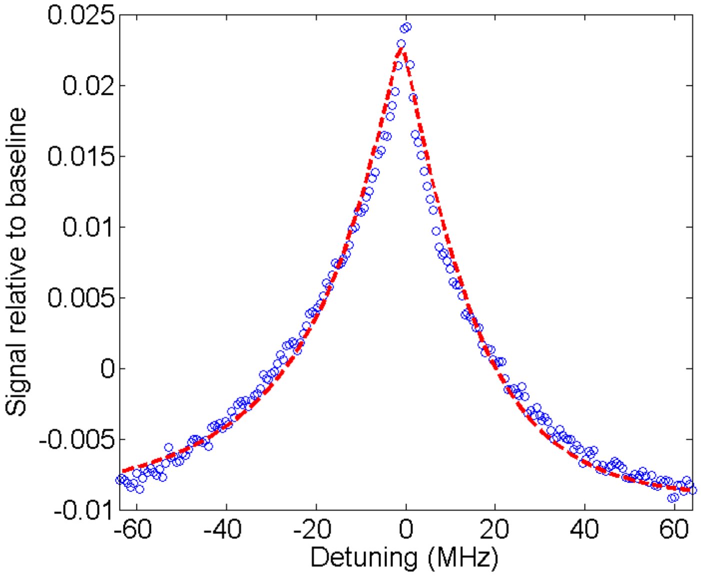

Figure 4.4: Data (blue circles) and theoretical fit (red dashed line) for the trace in Fig. 4.3 corresponding to $\theta - \theta_c \approx 4.68$ mrad.

The line narrowing mechanism of *Ramsey-narrowing* was proposed in Refs. [59, 60, 61] as a way to describe observed EIT lineshapes when power broadening of the line is negligible. The idea is that atoms that are coherently prepared by the probe and the control fields can diffuse out of the two fields and evolve for a time “in the dark”. They can then diffuse back into the fields, although the phase that they will have accumulated during that time will be different for different detunings and different times spent in the dark. When the atoms return to the fields, their coherences can interfere and produce fringes analagous to Ramsey fringes. In a thermal vapour the fringes wash out and result in a lineshape where a sharp central feature sits on a broader pedestal. The resulting lineshape is very similar to what we observe in our system. In fact, it is so similar that one might be tempted to describe the lineshape as entirely being due to Ramsey-narrowing. This is likely not the case, although the reader will have to wait until a later section for the reason. That being said, there may be some contribution to the cusp due to the Ramsey-narrowing process.

4.3 Lineshape characteristics

In standard vapour cell EIT experiments the linewidth of the EIT transmission peak is often of great interest. For slow light and optical memories, the width, combined with the contrast and optical depth, determines the group velocity of a probe pulse propagating under EIT conditions as well as the lifetime of any stored excitation. Given a particular cell length, the group delay can be calculated and the feasibility of storage determined. For applications as a frequency standard, the width of the transmission line in addition to the contrast determine the frequency stability of the system. Finally, the behaviour of the linewidth of the peak as a function of different parameters of the system provides insight into the primary decoherence mechanisms. In this section, I will describe two different linewidth measurements that we performed and their consistency with our simple model.

In many EIT experiments the lineshape is Lorentzian, and there is only one width to measure: the full-width at half-maximum (FWHM). If the lineshape is not a Lorentzian, as is the case with our experiment, the notion of a single width becomes less useful. Non-Lorentzian lineshapes can arise when there are two or more different mechanisms that contribute in different ways to the ground-state decoherence, as opposed to the ideal case where all decoherence mechanisms – such as magnetic field inhomogeneities and power broadening – contribute in exactly the same manner. Such similarity preserves the Lorentzian lineshape. We characterize our EIT lineshapes using two widths: the width of the cusp and the width of the pedestal. We can measure the width of the pedestal in two different ways. The first is to record the reflectivity and then directly measure the FWHM of the signal. The second method is to measure the phase shift of the probe field using the method described in Sec. 3.4. The width is then defined as the frequency difference between the maximum and minimum of the phase profile. For a Lorentzian, the FWHM as measured from the transmission is exactly the same as the width measured using the phase. We define the width of the cusp as being the frequency separation between the two inflection points of the reflectivity. We measure this by using an electronic differentiating circuit to differentiate the voltage from the photodiode: this results in a signal that is proportional to the derivative of the lineshape and hence the derivative of the effective susceptibility. The width is then defined in a similar fashion to that measured by the phase, except the width measured using the inflection points for a perfect Lorentzian is a factor of $1/\sqrt{3}$ smaller than the FWHM. In order to make comparisons between the width of the pedestal measured using the FWHM and the width of the cusp measured using the derivative, we multiply the derivative width by $\sqrt{3}$ to get an effective FWHM for the cusp.

4.3.1 Variation of width with control field power

To start off, let us use the theory developed in Sec. 2.6 to determine how the two widths should vary with the control field power. I find the variation of the width of the cusp by taking two derivatives of Eq. 2.36, setting the imaginary part to zero and solving for the corresponding detunings. In the limit of $\Delta_c = 0$ and $\Gamma \gg \delta, \gamma$ the resulting effective FWHM W_{Cusp} is

$$W_{\text{Cusp}} = 2\gamma \frac{(1 + 2\frac{\Omega_c^2}{\Gamma'\gamma})}{\sqrt{1 + \frac{4}{3}\frac{\Omega_c^2}{\Gamma'\gamma}}}. \tag{4.1}$$

In the regime of low power $\Omega_c^2/\Gamma'\gamma \ll 1$ the above expression reduces to

$$W_{\text{Cusp}} \approx 2\gamma + \frac{8}{3}\frac{\Omega_c^2}{\Gamma'} \tag{4.2}$$

which is linear in the control field power. The linearity of the width is expected based on the model of pure ground-state dephasing rather than population exchange [38], although in the evanescent case the width increases slower with power than in the case for pure travelling waves in regular EIT experiments. The reason is that the control field Rabi frequency here is measured at the interface, whereas the majority of atoms see a Rabi frequency that is smaller due to its decay into the vapour. Outside of the low power regime, the width of the cusp scales as the square root of the control field power. Since the cusp itself is due to atoms that see a very weak control field power ($\Omega_c^2/\Gamma'\gamma \ll 1$), it should be independent of Ω_c. However, the atoms that are only a little bit closer to the interface will contribute a lineshape that has some variation with Ω_c, and this will in turn affect the linewidth of the cusp.

Since in our model the pedestal is due entirely to power broadening of the transmission line, we expect that its width should vary roughly linearly with an intercept at 2γ. To determine the variation of the pedestal width with Ω_c, we have to solve for the locations of the half-maxima of Eq. 2.36. The maximum value of $\Im(\chi_{\text{eff}})$ is approximately $2/\Gamma'$, and the minimum value, when $\delta = 0$, is $\frac{\gamma}{\Omega_c^2} \log\left(1 + \frac{2\Omega_c^2}{\Gamma'\gamma}\right)$. The problem that we have to solve is then to find δ_{FWHM} such that

$$\Im\left(\chi_{\text{eff}}(\delta_{\text{FWHM}})\right) = \frac{1}{\Gamma'} + \frac{\gamma}{2\Omega_c^2} \log\left(1 + \frac{2\Omega_c^2}{\Gamma'\gamma}\right). \tag{4.3}$$

The above equation does not have an analytical solution, so instead I have plotted the widths of both the cusp and the pedestal in Fig. 4.5. As seen in the figure, the width of the pedestal is roughly linear with a slope of 1.984γ. This scaling is also less than what is found in regular EIT

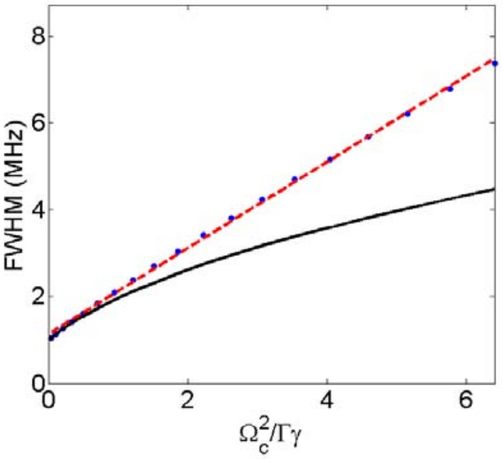

Figure 4.5: Width of the evanescent EIT transmision peak as a function of $\Omega_c^2/\Gamma'\gamma$. The black solid line is the effective FWHM of the cusp, the blue circles are the FWHM of the pedestal as obtained from Eq. 4.3, and the red dashed line is a linear fit to the data for the FWHM of the pedestal. The parameters used in this plot are $\Gamma = 2\pi \times 500$ MHz and $\gamma = 2\pi \times 0.5$ MHz.

experiments, and again this can be understood because Ω_c in Eq. 2.36 is the control field Rabi frequency at the interface which is higher than its value in the atoms. Note that the scaling of the width with power is only roughly linear: there is a slight curvature to the theoretical values.

The experimental data for the widths of the transmision line are shown in Fig. 4.6. The first thing to notice is that we can obtain a cusp linewidth that is smaller than the natural linewidth of the system which indicates that coherent effects are present rather than optical pumping. Both measured widths have linear scalings with the control field power (and hence Ω_c^2), even though the width of the cusp should show a distinct sub-linear scaling. As can be clearly seen in Fig. 4.6, the fit to Eq. 4.1 poorly describes the data. The ground-state dephasing that the fit predicts is about 20 kHz which is much less than the lowest measured linewidth of the cusp. The linear fit to the cusp width predicts a ground-state dephasing rate of 1.3 MHz which is more consistent with the measured values. As a further issue, the intercepts of both linear fits are different. From the theory, one would expect that in the limit of low power both the cusp and pedestal widths should be the same. The fact that the pedestal intercept is 12.6 MHz rather than 1.3 MHz is concerning. Thus, we have a situation where we have a good theoretical fit to

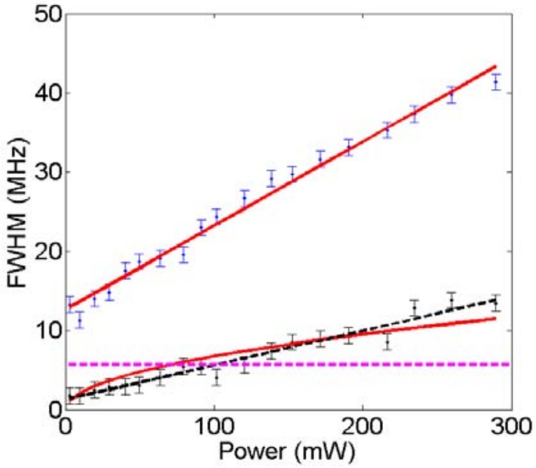

Figure 4.6: Widths of the EIT transmission line as a function of control field power. The black crosses are the measured widths of the cusp with a linear fit (solid red line). The blue dashed line is a fit to Eq. 4.1. The blue circles are the measured widths of the pedestal, also with an associated linear fit. The dashed magenta line indicates the FWHM of the D1 transition in ^{87}Rb .

the spectra in Fig. 4.3, but the data do not vary with the control field power in the same way that we would expect. One resolution to this inconsistency is that because we independently fix the amplitude and Ω_c in the fits, Ω_c controls only the width of the transmission peak. Therefore, if we were to vary the control field power and then fit each spectrum, we would find that even at very low power there is an anomalously large value for Ω_c which would account for the residual width.

4.3.2 Effects of diffusion

The above comparison between experimental data and theory suggests that further effects in the system need to be considered. The most obvious effect that should be included is the motion of atoms into and out of the interaction region. In our system, which contains a significant vapour pressure of buffer gas, the rubidium atoms move diffusively in the cell. This raises the possibility of Ramsey narrowing, where the atomic coherence can evolve in the dark before returning to the probe field. The lineshape that is measured will also show a cusp feature which is limited by the ground-state dephasing, and a broad pedestal which is a combination of power broadening and transit time effects. The original treatment of Ramsey narrowing assumed top-hat beams, so that the effects of spatially varying EIT linewidths would not need to be considered [59]. In our case, the spatial variation of the EIT linewidth is very important, so a different model needs to be used. A more general model for the effect of diffusion on EIT is described by Firstenberg *et al.* [51], so I will not give a derivation here. I shall simply give the relevant result that the ground-state coherence should obey

$$D\frac{\partial^2 R_{cb}(z)}{\partial z^2} = (\gamma - i\delta + K|\Omega_c(z)|^2)R_{cb}(z) + NK\Omega_c^*(z)\Omega_p(z) \tag{4.4}$$

where D is the diffusion constant (approximately 3 cm^2/s for a buffer gas pressure of 50 Torr [60]), K is the one-photon spectrum (in our case $K = i[\Gamma'/2 - i(\Delta_c + \delta)]^{-1}$) and $R_{cb} = N\rho_{cb}$ is the density corresponding to the ground-state coherence (see Fig. 2.1). The relevant boundary conditions in this case are that $R_{cb}(0) = 0$ due to wall collisions, and that $R_{cb}(z \to \infty) = 0$ due to the decaying fields. The ground-excited state coherence, which determines the probe spectrum, is then

$$R_{ab}(z) = iK(\Omega_c(z)R_{cb}(z) + N\Omega_p(z)). \tag{4.5}$$

An instructive case is to solve Eq. 4.4 when the fields are uniform in order to see how the ground-state coherence changes as one gets farther from the interface. The boundary conditions are different in this case as compared to evanescent fields, in that we cannot require that $R_{cb}(z \to \infty) = 0$, as the fields themselves are infinite. However, we can insist that the coherence does not blow up as $z \to \infty$, and the solution is

$$R_{cb}(z) = \frac{NK\Omega_c^*\Omega_p}{\gamma - i\delta + K|\Omega_c|^2}\left[\exp\left(-z\sqrt{\frac{\gamma - i\delta + K|\Omega_c|^2}{D}}\right) - 1\right]. \tag{4.6}$$

The important fact to notice is that the coherence starts from zero and then reaches its maximum value in a length scale given by $z_0 = \sqrt{\frac{D}{\gamma + 2\Omega_c^2/\Gamma}}$. Atoms within z_0 of the interface do not contribute significantly to the coherence, and the size of that 'null' region is related to the power-broadened EIT linewidth. As one drives the atoms harder with the control field, they relax to the dark state sooner after colliding with the interface, and this narrows the null region. Although one should be careful when extrapolating the spatially uniform field result to the spatially varying field problem, one can intuitively see that in the evanescent case the atoms that should nominally contribute the widest and highest contrast transmission line – those near the interface – will in fact contribute very little to the measured EIT profile. This will have the result of creating a narrower pedestal relative to the cusp than what we would predict when we ignore diffusion.

In analogy to Ramsey narrowing, in evanescent EIT we will also have effects due to transit-time broadening. In contrast to atoms that start off in the beam, diffuse out for a time, and then return, some atoms diffuse through the beams once and interact with the fields for only a short period of time. They will therefore contribute to a pedestal whose width is determined mainly by power broadening in the high-power regime and transit-time broadening in the low power regime. Therefore, the linewidth of the pedestal should still be roughly linear in Ω_c^2, but it should have an intercept that is larger than the ground-state dephasing rate. To make a comparison, I numerically solve Eq. 4.4 for R_{cb}, calculate the susceptibility as $\chi = \frac{d^2 R_{ab}(z)}{\hbar\epsilon_0\Omega_p}$, and compute the effective susceptibility using Eq. 2.35. A plot of the two different widths of the EIT transmission line using the above theory is shown in Fig. 4.7. Here, we see that the width of the pedestal has a linear dependence on Ω_c^2 with an intercept that is larger than the ground-state dephasing rate, as we see for experimental data in Fig. 4.6. However, the width of the cusp shows no variation with Ω_c^2. The physical reason for this is that the cusp is primarily due to Ramsey narrowing, and not due to power broadening, so it enjoys isolation from the pedestal. Of course, in Fig. 4.6 the width of the cusp does indeed vary. This discrepancy suggests that a more complicated mechanism than either diffusion-induced Ramsey narrowing or simple spatial variation of the EIT power broadening is responsible for the observed line shape and its behaviour.

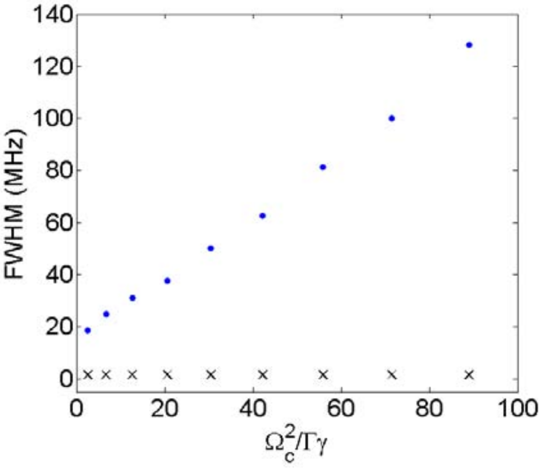

Figure 4.7: Pedestal (blue circles) and cusp width (black crosses) of the EIT transmission line when diffusion is included. The angle (and hence the interaction region size) was chosen to be $\theta_c + 0.05°$.

4.3.3 Variation of width with incident angle

The second investigation we performed on the widths of the EIT transmission line was to measure the widths as a function of the incident angle of the fields. Since the penetration depth (skin depth) of the fields is $(k_0\eta)^{-1}$, this measurement is equivalent to measuring the width as a function of the size of the interaction region. Our theory, neglecting diffusion, predicts that the widths of the pedestal and cusp should vary only slightly with the incident angle, and that variation should be due to variation in the control field transmission and Doppler broadening parallel to the interface. In the low-power regime, the width of the cusp should not vary at all because its width is determined by the ground-state dephasing rate.

The results of our measurements are shown in Fig. 4.8. As is clearly seen, neither width varies significantly over a wide range of incident angles and therefore interaction region sizes. For the largest incident angle shown, the size of the interaction region is about 1 μm. There is substantial variation near the critical angle, but that is because the lineshape starts to take on a dispersive appearance as seen in Fig. 4.2.

Contrast the negligible variation of either width with the variation predicted by a theory

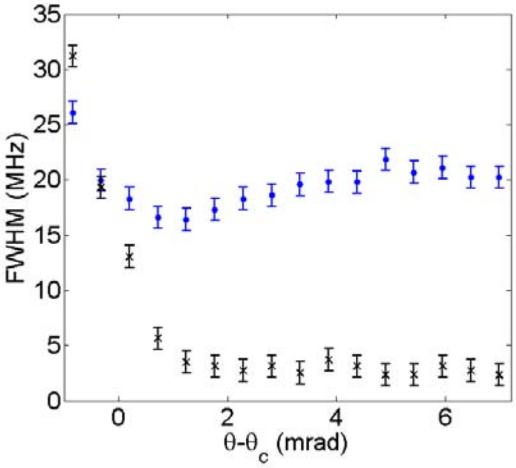

Figure 4.8: Widths of both pedestal (blue circles) and cusp (black crosses) as a function of the incident angle with a control field power of approximately 70 mW. The steep rise in the width near the critical angle is due to the reflectivity no longer resembling a transmission window.

that includes diffusion, as shown in Fig. 4.9. Again, the width of the cusp does not vary with

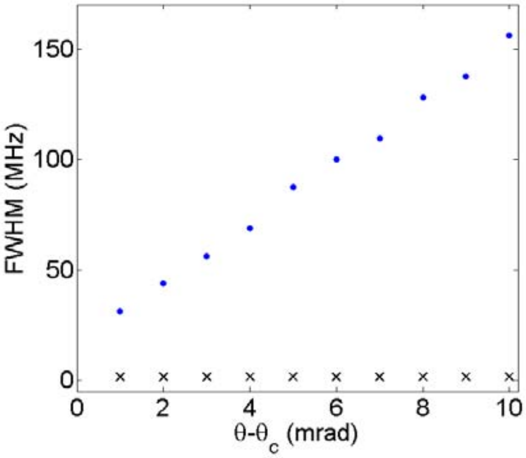

Figure 4.9: Widths of cusp (black crosses) and pedestal (blue circles) as a function of incident angle for $\Omega_c = 2\pi \cdot 50$ MHz s^{-1} when diffusion is included in the model.

the angle. However, the width of the pedestal is significantly affected by the motion of atoms over the range of angles that we consider. In fact, the width of the pedestal appears to be linear in $\theta - \theta_c$; a fact we can deduce from simple arguments. If the size of the interaction region is $(k_0\eta)^{-1}$, then the broadening associated with the transit of the atoms is, within a constant factor, $Dk_0^2\eta^2 \approx Dk_0^2(\theta - \theta_c)$ near θ_c.

The result that the widths of the EIT line are independent of the size of the interaction region is very surprising, as one would expect that in an interaction region this small the motion of atoms would play a major role. It apparently does not. This suggests a rather interesting application of this system as a compact optical frequency standard. Given that the size of the interaction region only needs to be a couple of microns, one could imagine creating a vapour cell that is only about 10 microns across and using the evanescent fields to generate an EIT signal with a cusp width less than the natural linewidth of the D1 transition. Suitable lock-in detection could be used to generate an error signal and the control and probe fields could be stabilized to one another. Similar compact frequency standards have been proposed based on micro-metric vapour cells, and in the majority of cases the narrowest linewidth that could be achieved was on the order of 10 MHz [31, 32, 33], although one study achieved a linewidth of 175 kHz [34].

The main problem with such an application is how to limit the ground-state dephasing rate which leads to a cusp width of about 1 MHz in our system. Since diffusion appears to play no significant role in the behaviour of the transmission lineshapes, we must look to other explanations. Suggestions have been made that the decoherence is due to Rb-Rb spin exchanging collisions, but a quick calculation shows that this is unlikely. The expected broadening associated with such collisions is [62]

$$\gamma = N\sigma_{\text{ex}}\bar{v}_{\text{rel}} \tag{4.7}$$

where σ_{ex} is the spin exchanging cross-section and $\bar{v}_{\text{rel}}$ is the average relative speed between the atoms. Using $\sigma_{\text{ex}} \approx 10^{-14}$ cm^2 [63], $\bar{v}_{\text{rel}} \approx 180$ m/s and $N = 6.0 \times 10^{18}$ m^{-3} (given by our spectra), I find that $\gamma/2\pi \approx 200$ Hz. This value is much less than the measured decoherence rate, and therefore Rb-Rb spin exchanging collisions are not likely to be the cause of the observed decoherence. A more likely option is that the decoherence is due to spin-flipping collisions with the interface. We could imagine using a paraffin or alkene coating on the interior of the cell in order to reduce the decoherence associated with wall collisions [64]. One problem with such coatings, however, is that they tend to degrade above about $100°$C, whereas we operate our oven at $170°$C. Using suitable lock-in detection methods, one might be able to detect an EIT signal at the lower temperature, but then the stability of a potential frequency reference might be compromised by the lower signal-to-noise [34].

4.4 Group Delay

No discussion of EIT would ever be complete without some measurement of slow light; slow light, of course, being one of the main reasons people are interested in EIT. In most slow light experiments, one sends a pulse through an EIT medium and measures the delay of the pulse (the group delay), and from that and a measurement of the length of the medium one can infer the group velocity. In general, the group velocity is

$$v_{\text{gr}} = \frac{d\omega}{dk} = \frac{c}{1 + \frac{\omega}{2}\Re\left(\frac{d\chi}{d\omega}\right)} \tag{4.8}$$

when the susceptibility is much less than unity. For the case of so-called normal dispersion $d\chi/d\omega$ is postive, and there is a reduction in the group velocity. One can also infer the group delay by measuring the phase shift ϕ of continuous-wave fields as a function of frequency. The group delay is then directly computed as

$$\tau_{\text{gr}} = \frac{\partial\phi}{\partial\omega}, \tag{4.9}$$

and the expression is evaluated at the two-photon resonance.

The benefit of EIT is that one can achieve a narrow linewidth transparency window with a correspondingly large $d\chi/d\omega$. For an EIT medium, the group velocity is given by

$$v_{\text{gr}} = \frac{c}{1 + \frac{Nd^2\omega}{2\hbar\epsilon_0}\frac{4\Omega_c^2}{\Gamma^2(\gamma + 2\Omega_c^2/\Gamma)^2}} \tag{4.10}$$

so for large N and small γ one can achieve significant reduction in the group velocity. Typical group velocities in warm vapour cells are around tens of km/s, although some studies have achieved group velocities on the order of 10 m/s [65]. The fact that the group velocity is regulated by the control field leads to the application of EIT as a optical quantum memory: one can turn the control field off while the pulse is inside the medium, and the pulse will stop and be converted into an atomic excitation that can be retrieved later [9]. In order for this to work, the incident pulse must fit entirely inside the medium. The pulse is compressed since there is a significant reduction in the group velocity, and the condition for the pulse to fit inside the cell is that $\tau < L/v_{\text{gr}} = \tau_{\text{gr}}$ where τ is the temporal extent of the pulse and L is length of the EIT medium. This is equivalent to requiring that the pulse be delayed by at least a pulse length. Furthermore, one wants the pulse to fit entirely inside the transmission window: this means one would like $\tau > W^{-1}$ where W is the width of the transmission window. These are two important conditions for storage of light in EIT.

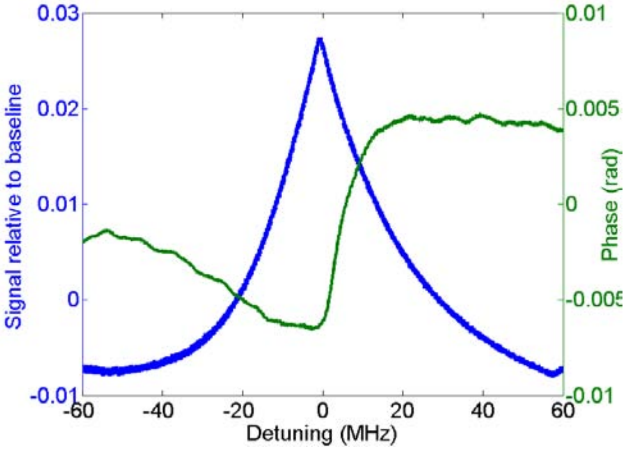

Figure 4.10: Measured reflectivity (blue) and phase (green) of the glass-vapour interface.

In our experiment the concept of a propagation length L is fuzzy, and so too is the idea of a group velocity. Exactly where is the pulse propagating? However, the notion of a group delay is still well-defined. The reflection coefficient for $\theta > \theta_c$, defined by Eqs. 2.34 and 2.36, is

$$r = r_0 \left(1 + \frac{i n_1 b}{\eta (n_1^2 - 1)} \chi_{\text{eff}} \right), \tag{4.11}$$

so the probe field will experience a phase shift due to the atoms that is given by

$$\phi = \frac{in_1 b}{\eta(n_1^2 - 1)} \Re\left(\chi_{\text{eff}}\right) \tag{4.12}$$

in the limit that $\chi_{\text{eff}} \ll 1$. Using Eqs. (4.9) and (4.12) at $\delta = 0$ and when the linewidth is much smaller than Γ', we have that the group delay is

$$\tau_{\text{gr}} = \frac{in_1 b}{\eta(n_1^2 - 1)} \frac{Nd^2\sqrt{\pi}}{\hbar\epsilon_0} \left(\frac{1}{\Omega_c^2} \log\left(1 + 2\frac{\Omega_c^2}{\Gamma\gamma}\right) - \frac{2}{\Gamma(\gamma + 2\Omega_c^2/\Gamma)} \right). \tag{4.13}$$

We measure the phase profile of the reflected signal as a function of the detuning as described in Sec. 3.4; an example of a phase profile is shown in Fig. 4.10. We measure the slope (divided by 2π) at the center of phase profiles such as the one in Fig. 4.10, and this provides a reasonably robust method for inferring the group delay that a pulse would experience after being reflected from the interface. We also directly measure the group delay of pulses that are reflected from the interface, and both types of measurements are consistent with one another. Inferring the group delay from the phase profile is preferable, however, because the group delay is very small compared to the duration of pulses that we can generate, and thus measuring the group delay with pulses is not very precise. The group delay as a function of power is shown in Fig. 4.11. We fit to Eq. 4.13 by changing only the x and y scales, and we see that the theory describes the data reasonably well. Note, however, that the scale of the group delay is on the order of 100 ps. The maximum group delay that we have ever achieved is around 500 ps at a control field power of about 100 mW and $\theta - \theta_c \approx 1$ mrad. In regards to the storage criterion discussed above, any pulse that we wished to store would have to have a duration less than 500 ps. At the same time, the pulse would have to have a bandwidth of less than about 10 MHz corresponding to a duration of about 160 ns. The two disparate time scales strongly imply that efficient storage is impossible with this system. A rough estimate of the expected efficiency yields $0.5/160 \approx 0.3\%$, which explains why our attempts at showing storage have never shown recall of any fraction of light.

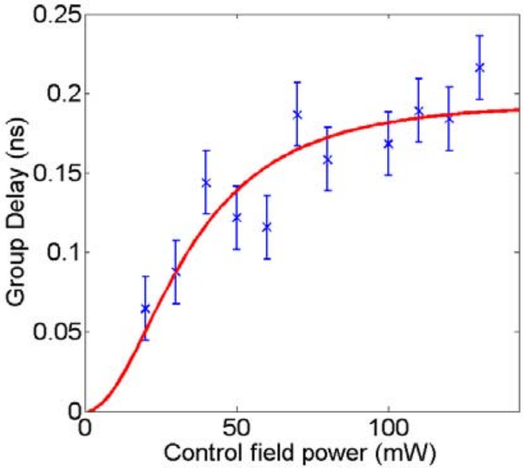

Figure 4.11: Group delay inferred from phase profiles as a function of the control field power (blue crosses) and a fit to Eq. 4.13. Error bars are estimates of the replicability of the data points.

4.5 Measurement of the Goos-Hänchen shift

As a final result, we made a very preliminary measurement of the contribution of EIT to the GHS using the measurement technique described in Sec. 3.5. Figure 4.12 shows the reflectivity spectrum and the lateral GHS for several angles near critical. For angles that are larger than the critical angle, we measure beam shifts that have dispersive appearances in accordance with the second term in Eq. 2.52. At the critical angle the GHS is distinctly peaked at the two-photon resonance. Below the critical angle we find that the beam shift does not take on a peaked structure as would be expected, but it instead remains as a dispersive shape that looks suspiciously similar to the actual reflectivity. Recall from Sec. 3.5 that the signal measured by the balanced detector is proportional to the product of the power in the reflected beam and its position relative to center. If we do not correctly account for the reflectivity, then we do not expect a correct measure of the beam position. Incorrect balancing of the detector, for instance, would lead to us to measure a combination of the signal from the beam shift and from the reflectivity. In comparison, the beam shifts measured for angles above the critical angle do not strongly resemble their respective reflectivities, so we conclude that we are measuring the actual beam shift. Note that for angles very far above the critical angle (not shown) the measured beam shifts begin to resemble their reflectivities, so again the signal caused by the beam shift is simply far smaller than the changes in power.

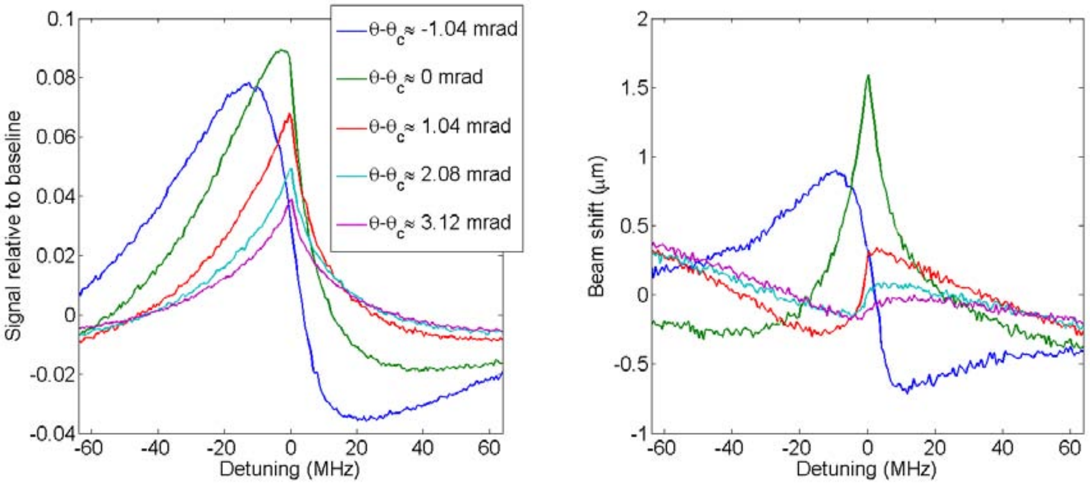

(a) Reflectivity of the interface as a function of detuning for several different angles near critical. Data is from the same set as shown in Fig. 4.3.

(b) Measured beam shift as a function of detuning and angle. Curves with the same color between right and left figures correspond to the same angle.

Figure 4.12: Reflectivity and GHS spectrum of the interface.

In principle, one could attempt to fit the data in Fig. 4.12(b) to Eq. 2.52. In practice, it is not worth the effort. Only a few curves behave as one would expect if the signal was due to only a beam shift and not due to variations in reflectivity as well. Further, the GHS is really only significant near the critical angle where the theory that I have been using throughout this thesis fails. Only a couple of the beam shift curves are well described by the simple model, but the parameters that describe those curves in the context of the model are very different. Furthermore, the beam shift measurements show a linear variation with frequency that cannot be explained solely with the Doppler broadened absorption spectrum. I conclude from these observations that our model does not describe our data well. Several issues with the experiment could contribute to some of the observed problems. The pick-off mirror does not exactly split the beam fifty-fifty. Much of the beam power is lost at the edge of the mirror, and this is hard to predict in advance, so that the calibration of how much power reaches the balanced detector is very difficult. Use of a split photodiode and servo motor, as in Pfleghaar *et al.* [28], could reduce the uncertainty in the changing reflectivity of the interface. Also, leakage of the control field through the polarization filtration optics contaminates the measurement of the GHS by unbalancing the detector which contributes to our imperfect ability to account for the changes in reflectivity. Lastly, the hot oven creates air currents that significantly deflect the probe beam making measurements of beam shifts difficult to do. Even with a lens to nominally remove such angular deviations, a great deal of averaging has to be done to achieve good signal-to-noise. If the voltage in a specific waveform exceeds the oscilloscope's range, then the averaged signal will be distorted and will not be a true measure of the beam shift. These problems would need to be addressed in further experiments.

Chapter 5

Conclusion

In this thesis, I have described our experiment to observe and characterize EIT using the technique of selective reflection. I first developed a basic theory in Chapter 2 that describes how the presence of the non-linear EIT interaction modifies the reflectivity of a glass-vapour interface. For angles below the critical angle, the EIT lineshape mimicked the real part of the regular EIT susceptibility. For angles above the critical angle, the evanescent control field created a depth-dependent EIT linewidth which resulted in a non-Lorentzian transmission peak in the reflection spectra. This lineshape is characterized by a sharp cusp that sits on a much broader pedestal. The basic model developed in Chapter 2 agreed reasonably well with the lineshapes, although it failed near the critical angle and it also failed to completely describe the cusp feature present in the transmission peaks. Measurements of the EIT linewidths as a function of power and angle showed partial agreement with the model. Attempts to better describe the data by including diffusion led to us excluding diffusion from playing a role. Surprisingly, we found that EIT persisted down to interaction region sizes of about 1 micron. We also measured frequency-dependent beam shifts that show the dependence of the GHS on EIT conditions.

Several improvements could be made to the apparatus. Firstly, rather than creating a prism-cell interface by using two separate elements and index-matching gel, we could instead have a single piece of glass manufactured that would consist of a standard vapour cell with a prism being one of the windows. Furthermore, the cell would be custom made for the particular purpose of evanescent EIT, so we would not need anti-reflection coating and therefore the reflectivity of the interface would actually be known. Another improvement would be in the design of the oven. Currently, the interface sits slightly outside the oven making the interface colder than the rest of the cell. This design results in significant formation of rubidium condensation on the interface which limits the contrast of the EIT signal. Ideally, one would have an oven where the entire cell is inside the oven and kept at a constant temperature with perhaps a cold finger to promote rubidium condensation away from the interface.

The major application of this work is as a compact optical clock. We have demonstrated linewidths of less than the natural linewidth of the system, and those widths appear to be limited by collisional decoherence. The use of a paraffin coated cell may significantly decrease the decoherence rate, although we might need to work at lower temperatures and thus lower signal-to-noise. Thus, there is potential to create a compact clock that is comparable in stability to micro-metric thin cells but in an easier-to-manufacture system.

Bibliography

[1] A. I. Lvovsky. Omnidirectional superfluorescent transients, 1998.

[2] K. J. Boller, A. Imamoglu, and S. Harris. Observation of electromagnetically induced transparency. *Physical Review Letters*, 66(20):2593–2596, May 1991.

[3] B.S. Ham, P.R. Hemmer, and M.S. Shahriar. Efficient electromagnetically induced transparency in a rare-earth doped crystal. *Optics Communications*, 144(4-6):227–230, December 1997.

[4] M. Baur, S. Filipp, R. Bianchetti, J. Fink, M. Göppl, L. Steffen, P. Leek, A. Blais, and A. Wallraff. Measurement of Autler-Townes and Mollow Transitions in a Strongly Driven Superconducting Qubit. *Physical Review Letters*, 102(24):243602, June 2009.

[5] Mika Sillanpää, Jian Li, Katarina Cicak, Fabio Altomare, Jae Park, Raymond Simmonds, G. Paraoanu, and Pertti Hakonen. Autler-Townes Effect in a Superconducting Three-Level System. *Physical Review Letters*, 103(19):193601, November 2009.

[6] G. S. Agarwal and Sumei Huang. Electromagnetically induced transparency in mechanical effects of light. *Physical Review A*, 81:041803, Apr 2010.

[7] J D Teufel, Dale Li, M S Allman, K Cicak, A J Sirois, J D Whittaker, and R W Simmonds. Circuit cavity electromechanics in the strong-coupling regime. *Nature*, 471(7337):204–8, March 2011.

[8] Jasper Chan, T P Mayer Alegre, Amir H Safavi-Naeini, Jeff T Hill, Alex Krause, Simon Gröblacher, Markus Aspelmeyer, and Oskar Painter. Laser cooling of a nanomechanical oscillator into its quantum ground state. *Nature*, 478(7367):89–92, October 2011.

[9] M. Fleischhauer and M. D. Lukin. Dark-state polaritons in electromagnetically induced transparency. *Phys. Rev. Lett.*, 84:5094–5097, May 2000.

[10] A. I. Lvovsky, Barry C. Sanders, and Wolfgang Tittel. Optical quantum memory. *Nature Photonics*, 3(12):706–714, December 2009.

[11] H. Schmidt and A. Imamoglu. Giant kerr nonlinearities obtained by electromagnetically induced transparency. *Opt. Lett.*, 21(23):1936–1938, Dec 1996.

[12] M. Nielsen and I. Chuang. *Quantum Computation and Quantum Information*. Cambridge University Press, 2000.

[13] Bing He, Andrew MacRae, Yang Han, A. I. Lvovsky, and Christoph Simon. Transverse multimode effects on the performance of photon-photon gates. *Physical Review A*, 83(2):022312, February 2011.

[14] E. Vetsch, D. Reitz, G. Sagué, R. Schmidt, S. T. Dawkins, and A. Rauschenbeutel. Optical interface created by laser-cooled atoms trapped in the evanescent field surrounding an optical nanofiber. *Physical Review Letters*, 104:203603, May 2010.

[15] Fam Le Kien and K. Hakuta. Slowing down of a guided light field along a nanofiber in a cold atomic gas. *Physical Review A*, 79(1):013818, January 2009.

[16] S. Spillane, G. Pati, K. Salit, M. Hall, P. Kumar, R. Beausoleil, and M. Shahriar. Observation of Nonlinear Optical Interactions of Ultralow Levels of Light in a Tapered Optical Nanofiber Embedded in a Hot Rubidium Vapor. *Physical Review Letters*, 100(23):233602, June 2008.

[17] J. Vanier. Atomic clocks based on coherent population trapping: a review. *Applied Physics B*, 81(4):421–442, July 2005.

[18] M. Klein, I. Novikova, D. F. Phillips, and R. L. Walsworth. Slow light in paraffin-coated Rb vapour cells. *Journal of Modern Optics*, 53(16-17):2583–2591, November 2006.

[19] J. Vanier, M.W. Levine, S. Kendig, D. Janssen, C. Everson, and M.J. Delaney. Practical realization of a passive coherent population trapping frequency standard. *Instrumentation and Measurement, IEEE Transactions on*, 54(6):2531 – 2539, December 2005.

[20] Eugeniy E. Mikhailov, Travis Horrom, Nathan Belcher, and Irina Novikova. Performance of a prototype atomic clock based on linlin coherent population trapping resonances in Rb atomic vapor. *Journal of the Optical Society of America B*, 27(3):417, February 2010.

[21] J. Guo, J Cooper, and A Gallagher. Selective reflection from a dense atomic vapor. *Physical Review A*, 53(2):1130–1138, February 1996.

[22] Ping Wang, A Gallagher, and J Cooper. Selective reflection by Rb. *Physical Review A*, 56(2):1598–1606, August 1997.

[23] B Gross, N Papageorgiou, V Sautenkov, and A Weis. Velocity selective optical pumping and dark resonances in selective reection spectroscopy. *Physical Review A*, 55(4):2973–2981, 1997.

[24] G. Nienhuis, F. Schuller, and M. Ducloy. Nonlinear selective reflection from an atomic vapor at arbitrary incidence angle. *Physical Review A*, 38(10):5197–5205, 1988.

[25] Rikio Kondo, Satoshi Tojo, Takashi Fujimoto, and Masahiro Hasuo. Shift and broadening in attenuated total reflection spectra of the hyperfine-structure-resolved d2 line of dense rubidium vapor. *Phys. Rev. A*, 73:062504, Jun 2006.

[26] F. Goos and H. Hänchen. Ein neuer und fundamentaler versuch zur totalreflexion. *Annalen der Physik*, 436(7-8):333–346, 1947.

[27] M Merano, A Aiello, M. P. van Exter, and J. P. Woerdman. Observing angular deviations in the specular reflection of a light beam. *Nature Photonics*, 3(6):337–340, May 2009.

[28] E. Pfleghaar, A. Marseille, and A. Weis. Quantitative investigation of the effect of resonant absorbers on the goos-hänchen shift. *Phys. Rev. Lett.*, 70:2281–2284, Apr 1993.

[29] Y B Ovchinnikov, S V Shul'ga, and V I Balykin. An atomic trap based on evanescent light waves. *Journal of Physics B: Atomic, Molecular and Optical Physics*, 24(14):3173, 1991.

[30] Yu. B. Ovchinnikov, I. Manek, and R. Grimm. Surface trap for cs atoms based on evanescent-wave cooling. *Phys. Rev. Lett.*, 79:2225–2228, Sep 1997.

[31] A. Sargsyan, C. Leroy, Y. Pashayan-Leroy, R. Mirzoyan, A. Papoyan, and D. Sarkisyan. High contrast D1 line electromagnetically induced transparency in nanometric-thin rubidium vapor cell. *Applied Physics B*, 105(4):767–774, July 2011.

[32] A. Sargsyan, D. Sarkisyan, and A. Papoyan. Dark-line atomic resonances in a submicron-thin Rb vapor layer. *Physical Review A*, 73(3):033803, March 2006.

[33] Y. Pashayan-Leroy, C. Leroy, A. Sargsyan, A. Papoyan, and D. Sarkisyan. Electromagnetically induced transparency: the thickness of the vapor column is of the order of a light wavelength. *Journal of the Optical Society of America B*, 24(8):1829, 2007.

[34] L Lenci, A Lezama, and H Failache. Dark resonances in thin cells for miniaturized atomic-frequency references. *Optics Letters*, 34(4):425, February 2009.

[35] Michael Fleischhauer, Atac Imamoglu, and Jonathan P. Marangos. Electromagnetically induced transparency: Optics in coherent media. *Rev. Mod. Phys.*, 77:633–673, Jul 2005.

[36] Marlan O. Scully and M. Suhail Zubairy. *Quantum Optics*. Cambridge University Press, Cambridge, 2002.

[37] Ali Javan, Olga Kocharovskaya, Hwang Lee, and Marlan O. Scully. Narrowing of electromagnetically induced transparency resonance in a doppler-broadened medium. *Physical Review A*, 66:013805, Jul 2002.

[38] E Figueroa, F Vewinger, J Appel, and A. I. Lvovsky. Decoherence of electromagnetically induced transparency in atomic vapor. *Optics letters*, 31(17):2625–7, September 2006.

[39] O. Firstenberg, M. Shuker, a. Ben-Kish, D. Fredkin, N. Davidson, and a. Ron. Theory of Dicke narrowing in coherent population trapping. *Physical Review A*, 76(1):013818, July 2007.

[40] David J. Griffiths. *Introduction to Electrodynamics, Third Edition*. Pearson Education, Inc., New Jersey, 2005.

[41] John David Jackson. *Classical Electrodynamics, Third Edition*. John Wiley & Sons, Inc., New York, 1999.

[42] David J. Griffiths. *Introduction to Quantum Mechanics, Second Edition*. Prentice-Hall, Inc., New Jersey, 1999.

[43] Chen-To Tai. *Dyadic Green's Functions in Electromagnetic Theory*. Intext Educational Publishers, Pennsylvania, 1971.

[44] S Kozaki and H. Sakurai. Characteristics of a Gaussian beam at a dielectric interface. *JOSA*, 68(4):508–514, 1978.

[45] J. Picht. Beitrag zur theorie der totalreflexion. *Ann. Phys. (Paris)*, 3:433, 1929.

[46] Rémi H. Renard. Total Reflection: A New Evaluation of the Goos-Hänchen Shift. *Journal of the Optical Society of America*, 54(10):1190, October 1964.

[47] John David Jackson. *Classical Electrodynamics, Third Edition*. John Wiley & Sons, Inc., New York, 1999.

[48] B. R. Horowitz and T Tamir. Lateral displacement of a light beam at a dielectric interface. *JOSA*, 61(5):586–594, 1971.

[49] J. W. Ra, H. L. Bertoni, and L. B. Felsen. Reflection and transmission of beams at a dielectric interface. *SIAM J. Appl. Math*, 24:396–413, 1973.

[50] Wojciech Nasalski. Longitudinal and transverse effects of nonspecular reflection. *JOSA A*, 13(1):172–181, 1996.

[51] O. Firstenberg, M. Shuker, R. Pugatch, D. Fredkin, N. Davidson, and A. Ron. Theory of thermal motion in electromagnetically induced transparency: Effects of diffusion, Doppler broadening, and Dicke and Ramsey narrowing. *Physical Review A*, 77(4):043830, April 2008.

[52] M. Shuker, O. Firstenberg, R. Pugatch, A. Ben-Kish, A. Ron, and N. Davidson. Angular dependence of Dicke-narrowed electromagnetically induced transparency resonances. *Phys. Rev. A*, 76:023813, Aug 2007.

[53] Ziauddin, Sajid Qamar, and M. Suhail Zubairy. Coherent control of the goos-hänchen shift. *Phys. Rev. A*, 81:023821, Feb 2010.

[54] D. Steck. Akali D line data. `http://steck.us/alkalidata/`.

[55] A. Macrae. Double electromagnetically induced transparency with application to nonlinear optics at low light levels, 2008.

[56] Jürgen Appel, Andrew MacRae, and A. I. Lvovsky. A versatile digital GHz phase lock for external cavity diode lasers. *Measurement Science and Technology*, 20(5):055302, May 2009.

[57] A. Vernier, S. Franke-Arnold, E. Riis, and A. S. Arnold. Enhanced frequency upconversion in Rb vapor. *Opt. Express*, 18(16):17020–17026, Aug 2010.

[58] Shen Yi-Fan, Dai Kang, Mu Bao-Xia, Wang Shu-Ying, and Cui Xiu-Hua. Energy-pooling collisions in rubidium: 5 p 3/2 +5 p 3/2 5 s +(nl = 5 d ,7 s). *Chinese Physics Letters*, 22(11):2805, 2005.

[59] Yanhong Xiao, Irina Novikova, David F Phillips, and Ronald L Walsworth. Repeated interaction model for diffusion-induced Ramsey narrowing. *Optics express*, 16(18):14128–41, September 2008.

[60] Yanhong Xiao, Irina Novikova, David F. Phillips, and Ronald L. Walsworth. Diffusion-induced ramsey narrowing. *Phys. Rev. Lett.*, 96:043601, Feb 2006.

[61] I Novikova, Y Xiao, D. F. Phillips, and R. L. Walsworth. EIT and diffusion of atomic coherence. *Journal of Modern Optics*, 52(16):2381–2390, November 2005.

[62] H. Warren Moos and Richard H. Sands. Study of spin-exchange collisions in vapors of Rb^{85}, Rb^{87}, and Cs^{133} by paramagnetic resonance. *Phys. Rev.*, 135:A591–A602, Aug 1964.

[63] Hyatt M. Gibbs and Robert J. Hull. Spin-exchange cross sections for Rb^{87}-Rb^{87} and Rb^{87}-Cs^{133} collisions. *Phys. Rev.*, 153:132–151, Jan 1967.

[64] M V Balabas, K Jensen, W Wasilewski, H Krauter, L S Madsen, J H Müller, T Fernholz, and E S Polzik. High quality anti-relaxation coating material for alkali atom vapor cells. *Optics Express*, 18(6):5825, March 2010.

[65] LV Hau, SE Harris, and Zachary Dutton. Light speed reduction to 17 metres per second in an ultracold atomic gas. *Nature*, 397(February):594–598, 1999.